Structures, 16 (2018), 358-372.

Monotonic and cyclic performance of threaded reinforcement splices

D.V. Bompa*, A.Y. Elghazouli

Department of Civil and Environmental Engineering, Imperial College London, UK

Abstract

This paper examines the fundamental uniaxial monotonic and cyclic response of reinforcement bars connected with threaded mechanical couplers. Based on a survey of available splicing forms, two types of threaded couplers with different geometric configurations, namely 'parallel threaded couplers' and 'parallel threaded sleeve couplers' are selected for detailed assessment. An experimental study consisting of twenty-four bare (in-air) and embedded (in-concrete) specimens incorporating threaded couplers and non-spliced counterparts, is described. The results enable direct assessment of strength as well as complete deformation characteristics, including the post-cracking and post-yield response, for both monotonic and cyclic conditions. After describing the material properties and specimen details, the main observations are reported based on detailed measurements of crack kinematics including crack width and spacing through a digital image correlation system. Complementary numerical studies, undertaken using nonlinear finite element procedures which are validated against the tests, enabled supplementary parametric investigations accounting for wider ranges of coupler geometries. The findings show that existing guidelines may be used for assessing the crack width and spacing, by accounting for the characteristic bond behaviour at the rebar and coupler regions. The complete deformational response may be obtained by using a suggested stiffness reduction factor that depends on the coupler geometry. Several 'in-air' performance parameters may also be used as a basis for the selection and implementation of couplers in applications requiring ductile member behaviour.

Keywords: Cyclic response; inelastic behaviour; concrete members; reinforcement splices; threaded mechanical couplers.

---

* *Corresponding author: Dr. D.V. Bompa*
E-mail: d.bompa@imperial.ac.uk

1. Introduction

Mechanical couplers for reinforcement splicing are recognised as an effective alternative to lapped or welded bars in reinforced concrete (RC) members, as these can overcome congestion problems whilst reducing material and constructional costs [1-6]. The reinforcement congestion becomes particularly critical for situations in which ductile detailing is necessary. Conventional lap splices can lead to over-reinforcement of the section, resulting in potential non-ductile response at the spliced region due to stress localisation at both ends of the lap, hence altering the deformation capacity [7,8]. In comparison to welded laps, mechanical splices are also more practical for site installation. The performance criteria of these systems are typically determined in terms of elastic slip, fatigue and strength considerations, using idealised 'in-air' uniaxial tests on reinforcement-coupler arrangements (e.g. [9,10]).

In-air monotonic tests on splices with Parallel Threaded Couplers (PTC) and Taper Threaded Couplers (TTC) show that whilst PTC typically fail outside the coupler region, TTC exhibit inferior performance with premature rebar failure at the threads, or complete strip-out of the threads [11-13]. Monotonic and cyclic tests on Upset Headed Couplers (UHC), indicate that failure occur in the reinforcing bar, and occur at significant ductility levels [14]. Swaged couplers (SWC) can exhibit brittle failure at mid-point of the coupling sleeve [15], in the rebar or gradual slip from sleeves [12]. Shear bolt lock couplers (BLC) generally exhibit lower strength and strain capacity compared to non-spliced bars due to fracture of the bars caused by stress concentration under the bolts [16]. Undesirable failure modes such as strip-out of the bar from the sleeve [17] can occur in offset bolt-lock couplers (OBLC) and complete slip from the sleeve has been reported in offset wedge swaged couplers (OSWG) tests [18]. Grouted sleeve couplers (GSC) generally develop full bar strengths, but the ductility of these splices can be up to 60% lower compared to non-spliced bars due to potential rebar-grout-sleeve slip [19-21].

Although 'in-air' tests are practical due to the simplicity of the testing, these do not represent directly the embedded 'in-concrete' behaviour, as the interaction between the concrete and rebar-coupler assembly may play a significant role in the performance. Also, in tension, the rebar-concrete bond stresses and reinforcement ratio affects the cracking kinematics, particularly the crack spacing [22]. Besides rebar-concrete adhesion characteristics and rebar-concrete frictional resistance, the bond capacity is strongly influenced by the surface type of the reinforcement bar (rebar) [23,24]. This aspect affects the reinforcement stress distribution, bond stress and slip distribution, as well as their interrelationships [25]. Most couplers have regular surfaces whilst most reinforcement bar surfaces are deformed. Additionally, the section size at the coupler is larger than that of the connected rebars,

resulting in a change in the local reinforcement ratio and a discontinuity in the member stiffness. Overall, the length, diameter, and surface conditions of couplers, in relation to those of the bars, may therefore be expected have a notable influence on the performance of RC members.

A recent comparative assessment of various forms of mechanical reinforcement splices, as illustrated in Figure 1, was carried out by the authors [26] based on a survey of over 350 'in-air' uniaxial splice tests considering the strength, ductility and geometry of couplers. It was shown that a strength criteria based on splice-to-bar ultimate capacity (i.e. $f_{u,sp}>f_{u,b}$) is not normally met in most systems, but is typically satisfied when based instead on splice-to-bar yield capacity (i.e. $f_{u,sp}>f_{y,b}$). In the absence of specific guidance for inelastic testing in current standards (e.g. [9]), a ductility criterion for use in dissipative zones [27] was proposed. This was expressed in the form of splice-to-bar ultimate strain ($\varepsilon_{u,sp}/\varepsilon_{u,b}$), and showed a clear difference between the performance of the coupling systems considered (Figure 2a) [26]. A 'size' parameter ($\lambda_s=d_cL_c/d_bL_b$) was used to characterise the geometry of the coupling system as shown in Figure 2b [26], where d_c and L_c represent the diameter and length of the coupler, respectively, whilst d_b and L_b are the diameter and effective length of the splice (L_c+4d_b), respectively. In principle, a favourable balance of 'in-air' strength and ductility, and low 'size-bulkiness', would have the potential for offering desirable inelastic 'in-concrete' performance.

In this paper, two types of tension-compression couplers, namely parallel threaded couplers (PTC) and cold forged sleeves with parallel thread couplers (PTSC), were selected for detailed assessment. In addition to the need in general for inelastic monotonic and cyclic assessment of threaded coupler systems, tests on RC members incorporating these specific coupler forms seem to be lacking. Uniaxial monotonic and cyclic 'in-air' and 'in-concrete' tests on PTC and PTSC, as well as non-spliced reference specimens, are carried out in this investigation for reinforcement bar diameters of 16 mm and 20 mm. A detailed study into the cracking kinematics of the concrete specimens is described, and comparisons with the response of the in-air counterparts are presented. After validation of nonlinear numerical procedures against the test results, parametric assessments are undertaken to provide insights into the stress and slip distributions, as well as comparative evaluations for different splice configurations. Based on the results, expressions are proposed for determining the cracked stiffness of concrete members incorporating mechanical splices. The experimental and numerical findings provide direct information on the inelastic cyclic response of in-air and in-concrete behaviour of mechanical splices and highlight the main design considerations for their practical application.

2. Experimental programme

2.1 Specimens and materials

To obtain a detailed insight into the in-air and in-concrete response of mechanical splices, uniaxial monotonic and cyclic tests were carried out using the parallel threaded couplers (PTC) and parallel threaded sleeve couplers (PTSC), illustrated in Figure 3, to connect 16 mm and 20 mm reinforcement bars. The PTC is a compact coupler with diameter d_c × length L_c = Ø25×45 mm for 16 mm bars and Ø31×54mm for 20 mm bars, while the PTSC has a diameter d_c × length L_c = Ø25×206 mm for 16 mm bars and Ø31×214 mm for 16 mm bars [28,29]. These are referred to throughout the paper as *compact* and *slender* couplers, respectively. The PTC splice is provided with standard female threads at the coupler and matching male threads at the rebars. The PTSC has matching male-female threads forged from a steel sleeve that is mechanically connected to the unaltered reinforcing bars. Through the fabrication process of these couplers, the cross-sectional area at the threads remains the same.

The in-air specimens subjected to monotonic loading had a minimum clear length l_s=350 mm between the testing machine jaws. As shown in Figure 4, the in-concrete specimens were made of an 800 mm long splice of which 600 mm was embedded in a concrete cylinder. For the splices made of d_b=16 mm rebars, the external diameter of the concrete cylinder was D_c=121 mm, whist for the d_b=20 mm rebars, the external diameter of the concrete was D_c=151 mm. This corresponds to a gross reinforcement ratio ρ_l=1.78% that is within the typical range for practical applications. As shown in previous studies, the bond properties and crack pattern are strongly dependent on the concrete cover. For members incorporating 16 mm bars, the concrete cover was 52 mm at the rebar and 48 mm at the coupler, whilst for members with 20 mm bars, the concrete cover was 65 mm at the rebar and 60 mm at the coupler. The concrete cover was chosen to minimise the occurrence of splitting failure along the embedded bars, maintain the same cover to rebar ratio (c/d) for all in-concrete specimens, whilst accounting for the experimental constraints. For both rebar diameters, the c/d=3.3, above the limits value at which splitting is expected to occur when no or little transverse confinement exists (c/d=1) [30] and above limits at which cover splitting can be completely neglected (c/d=3) [31]. The concrete specimens were cast vertically and kept in plastic forms for a week until their removal from forms.

Hot rolled deformed bars with diameters of 16 mm and 20 mm, made of steel Grade B500C and with a minimum relative rib area of 0.056, with surface treatment through sand blasting, were used for both uniaxial in-air and in-concrete tests. The actual relative rib area of each rebar size was assessed according to EN ISO 15630-1:2010 [32] using a digital calliper through measurement of external bar

diameters at ribs, between the ribs, perpendicular to, and at 45^o from the rib-to-rib axis. The rib inclination and projected rib length were measured from a print of a wet painted bar rolled on a sheet of paper. Details of the 16 mm and 20 mm rebar geometry are shown in Figure 5, whilst the material properties are given in Table 2. These types of reinforcement bars are widely used in UK practice and in research [33,34], and offer good bond response with bond parameters above 4.0 [35].

Cubes and cylinders samples from the ready-mix concrete used in the in-concrete specimens were prepared for determining the concrete mechanical properties. The samples were cast directly into plastic forms and covered with plastic sheets to facilitate concrete hydration until de-moulding the following day. Subsequently, the samples were submersed in water until they reached 28 days when they were removed and prepared for testing. The top and bottom faces of the Ø100×200 mm cylinders were ground to ensure surface flatness. All dimensions of the cylindrical samples were measured at a minimum of three locations and further averaged for assessment of strength. A minimum of four compression tests on 100 mm cubes and Ø100×200 mm cylinders (EN206-1:2000 [36]) and splitting tests on Ø102×254 mm cylinders at 28 days and at the time of testing were carried out. The 28 days concrete compressive strength was f_c = 44.8 MPa measured on cylinders and $f_{c,cube}$ = 51.4 MPa measured on cubes, whilst the splitting strength was $f_{ct,sp}$ = 2.92 MPa. The concrete strengths assessed at 60 days, which corresponds to the time of member testing were f_c = 53.3 MPa, $f_{c,cube}$ = 59.8 MPa and $f_{ct,sp}$ = 4.71 MPa.

2.2 Instrumentation and testing procedures

To assess elastic slip at the threads, three cycles between zero and 60% yield strength of the non-spliced counterpart were applied in the monotonic tests of the in-air mechanical splices. The same specimens were further subjected to a monotonically increasing axial displacement until fracture. After obtaining the complete stress-displacement σ-Δ curve from the monotonic test, for in-air or in-concrete specimens, the yield displacement Δ_y was extracted from the test data and used to determine the main characteristics for the cyclic loading procedure.

The cyclic in-air tests were subjected to the S2 low cycle reverse elastic-plastic loading pattern, as defined by ISO 15835-2:2009 [9] and illustrated schematically in Figure 6a. The loading procedure involves applying displacements Δ from zero up to $2\times\Delta_y$ (yield displacement) in tension followed by reversal corresponding to 50% of the yield strength in compression, alternating four times. Thereafter, the applied Δ is increased from zero up to $5\times\Delta_y$ in tension followed by reversal to 50% of the yield strength in compression, alternating again for four times. After the cycling is completed, the procedure involves applying increasing tension in the test specimen up to failure.

The in-concrete tests were subjected to a combined S1 and S2 low cycle loading test in which, initially the sample was subjected to 20 cycles from 90% of yield strength in tension to 50% of yield strength and compression as illustrated schematically in Figure 6b, followed by the S2 procedure described above (Figure 5a) [37]. Both the uniaxial in-air and in-concrete tests were carried out in an Instron 8802 testing machine provided with a capacity of 250 kN for dynamic loading (312 kN for static loading), as illustrated in Figure 7. The testing machine was provided with high-pressure jaws that restrain the clamped rebar region without permitting any slip.

A Digital Image Correlation (DIC) system, consisting of two cameras and a controller was used to capture crack propagation and member displacements, as this offers a high level of accuracy and practicality compared to conventional mechanical instrumentation [38,39]. High contrast black/white patterns were provided to the front face of the specimens by applying two layers of water-based white paint and, subsequently, a fine black speckle pattern. This procedure was required to allow the post-processing software to compute surface strain vector fields and subsequently strain values or crack width at required locations of the specimens by setting virtual gauges. The processed results provide detailed information about the crack pattern and development for concrete members, as well as strain localisation for both the steel and concrete specimens.

3. Results and observations

3.1 In-air specimens

The minimum tensile yield strength f_y, obtained from the non-spliced samples was 524 MPa for 16 mm and 508 MPa for 20 mm, whilst the ultimate strength f_u was 620 MPa and 617 MPa, respectively. Both f_y and f_u were assessed from the recorded load divided by the nominal bar area. The minimum ultimate mean strain ε_u, determined from the recorded displacement Δ divided by the clear length of the specimen was ε_u = 13.5% for 16 mm bars and ε_u = 14.1% for 20 mm bars. The test results in terms of yield force F_y and strength f_y, ultimate force F_u and strength f_u, mean strain at yield ε_y and ultimate mean strains ε_u and as well as a ductility factor determined as the ratio between ultimate-to-yield mean strains $\varepsilon_u/\varepsilon_y$, are all given in Table 2.

Figure 8 illustrates a comparison between the uniaxial deformation recorded by the non-spliced and in-air samples provided with couplers which may be used to determine the elastic slip at the couplers. As observed, both types of couplers had marginally higher deformation than the non-spliced reference bar with values below 0.2 mm. However, after the three elastic cycles, the residual deformation was

between 0.01-0.02 mm for all samples, showing that no slip developed at the couplers and that the higher deformation at peak occurred primarily due to the elastic elongation at threads.

Figure 9 depicts the stress-strain σ-ε response of the monotonic tests on the non-spliced and coupled rebars. As observed from these curves, all responses are within similar ranges with ε_u between 13.5-14.9%, whilst ε_y is nearly identical for each set of tests (16 mm and 20mm). The small differences at ultimate may be related to typical inherent material variations. It is worth noting that both coupling systems perform well under monotonic loading. The cyclic loading tests (S2) illustrated in Figure 9 show a consistent decrease in ε_u between the tested configurations. The non-spliced bars had the highest ε_u, in the range of 16% (15.6% and 16.2% for 16 mm and 20 mm, respectively) with splices with slender couplers having the highest decrease in ductility with ε_u of 10.3% for 16 mm and 8.8% of 20 mm splices. The splices with compact couplers reached ε_u of 13.4% and 10.3% for 16mm and 20 mm splices, respectively.

Figures 10a,b illustrate the longitudinal strain concentrations obtained from optical measurements at yield ε_y, half ultimate ($\varepsilon_u/2$) and ultimate ε_u. The intrinsic characteristics of the mechanical splices with compact couplers, that have an enlarged rebar cross-section near the threads due to the manufacturing process, have a beneficial influence on the strain distribution throughout the length of the splice with minimum stresses recorded at the coupler region. For slender couplers, some strain localisation occurs at the threads is also observed in the elastic slip response illustrated in Figure 8, as well as at the coupler to rebar interface in the inelastic regime which subsequently promoted a failure at the coupler region.

The above discussed reductions in ε_u occur at the splice level and may not characterise the coupler response. As illustrated in Figure 10c, the failure of the non-spliced rebars showed failure at the middle of the sample indicating a relatively uniform stress distribution and with minimal or no influence from the rebar clamping conditions. Considering a higher cross-section at the coupler in comparison to the rebar, the weaker section is transferred outside of the coupler. Consequently, higher straining is developed at the rebar, particularly when using slender couplers leading to shorter rebar regions, resulting in earlier failure which can occur near the coupler-to-rebar interface (Figure 10c). The reduction in ε_u between non-spliced-compact-slender splices may become proportionally less significant with the increase in total specimen length. This also needs to be considered carefully for bending elements incorporating relatively large couplers, as the moment gradient and possible concentration of plasticity in dissipative zones may also contribute to the reduction in ductility [40].

3.2 In-concrete members

The main results from the monotonic and cyclic tests on embedded mechanical splices are given in Table 3 in terms of cracking strength F_{cr}, yield strength F_y and ultimate strength F_u. The table also gives the corresponding overall yield ε_y and ultimate ε_u mean strains which, for qualitative comparisons purposes, are determined from the recorded machine displacement divided by the member clear length that includes the concrete region and free rebar region. A ductility ratio μ_ε, determined from the ultimate-to-yield mean strain ratio $\varepsilon_u/\varepsilon_y$, together with the elastic E_1 and cracked E_2 stiffness values, are also reported. A direct comparison between in-concrete members incorporating non-spliced and spliced Ø20 mm rebars, depicted in Figure 11 as a representative example, shows a consistent reduction in ε_u with splice type and type of loading. The ultimate strain ε_u is reduced under cyclic compared to monotonic loading by 21% for the member with slender coupler, by 15.7% for the member with compact coupler, and by 10% for the non-spliced member (Figure 11).

As for the in-air rebar tests, a similar trend regarding ε_u is obtained for the in-concrete members in both monotonic and cyclic tests, as shown in Figure 11 and Table 3. For example, the Ø20 members with slender couplers had lower ε_u in the range of 30%, whilst the compact Ø20 counterpart had lower ε_u around 20% compared to the non-spliced Ø20 counterparts. It is also worth noting that the uniaxial tests showed lower ε_u for in-concrete members in comparison with in-air specimens, contrary to indications from previous studies which imply that in-air response can be used as a conservative lower bound for splice performance [41].

3.2.1 Crack kinematics

The behaviour of the concrete members is typically characterised by an initial transverse crack, generally occurring around the member mid-span, followed by the opening of other transverse cracks, and ultimately by longitudinal cracks at the member extremities due to bond deterioration. Apart from one cyclic specimen with compact couplers and 16 mm rebars, which failed within the concrete region, all members failed due to rebar fracture in the free rebar region, outside of the bonded concrete region. Members with 16 mm and 20 mm, with the same rebar/splice configuration, developed similar crack patterns. Figure 12 illustrates typical crack patterns for representative 20 mm members, for both monotonic and cyclic cases, with more details provided for the latter for discussion purposes.

In the case of C0-20M (non-spliced), the first cracks developed at the centre of the member, with the left crack in Figure 12a growing gradually up to a member displacement Δ=20 mm. Although other cracks developed towards the member edge, most of the deformation was concentrated in the cracks recorded at ε_y, with values about twice that from other cracks. For CC-20M (with compact coupler)

shown in Figure 12b, transverse cracks developed outside the coupler region, showing that the coupler geometry had a largely insignificant influence on the crack distribution. For CS-20M (with slender coupler), crack initiation occurred within the coupler, yet outside the threaded section (Figure 12c). Equally spaced edge cracks developed after an applied displacement of $3\times\Delta_{y,}$ which subsequently governed the response near ultimate.

The behaviour of the C0-20C (non-spliced) was governed by two main cracks developing at about 1/3 and 2/3 of the member length, marked as No 1 and No 3 in Figure 12d. These propagated at the same rate within the elastic regime of the steel rebar, followed by a faster rate for Crack No 3 which had the widest opening at ultimate (w_{max}=18mm). For CC-20C (with compact couplers), Crack No 3 (located outside of the coupler length) and No 2 (at one bar diameter from the coupler) had similar rate of propagation, with No 2 governing the response up to Δ=20 mm. As shown in Figure 12e, beyond Δ=20 mm, edge crack No 1 took over, followed by No 4. For CS-20C (with slender coupler), Crack No 2 formed at the centre within the threaded section, governing the response up to about $4\times\Delta_y$; however, with the crack widths maintained below 2 mm up to ultimate. Subsequently, due to non-simultaneous extension of the rebar and concrete body, symmetric cracks developed towards the edge of the specimen after the last cycle of $2\times\Delta_y$ and governed the response up to ultimate (Figure 12f).

3.2.2 Crack widths

Figure 13a depicts the relationship between the experimental average crack widths $w_{m\,,}$ determined from optical measurements, and average reinforcement stress σ_{sm} up to w_m=0.5 mm, with values being within the elastic and yield regions of the rebar. On the other hand, Figure 13b shows the development of w_m in the inelastic range. Up to half yield $\varepsilon_y/2$, the average crack widths are shown to be within 0.1mm, exhibiting a steeper increase for CC-16M and CS-16M for which at yield $w_m\approx$0.25-0.30. In contrast, the remaining members show a more significant scatter up to $\varepsilon_y/2$, reaching $w_m\approx$0.1 at yield. It is worth noting that, CC-16M failed within the concrete bonded region, whilst the remaining members failed within the free rebar region. This is captured by the crack width-mean strain (w_m-ε) curves in Figure 13b that indicate wider average crack widths for CC-16M, with the other members grouped together up to ε=6.0%. Beyond this level of strain, members with slender couplers had lower w_m compared to the non-spliced members and those with compact couplers. The curves in Figure 13a,b suggest that prior to yield, the uniaxial behaviour of the tested configurations is very similar.

Figure 13c,d shows the average crack growth at key strain levels from the cyclic loading procedure. The average crack widths w_m are plotted at the first and last elastic cycles, at ε_y, $2\times\varepsilon_y$, and $5\times\varepsilon_{y,}$ and at around ε=5%. Compared to monotonic tests, within the elastic range of the rebar, the crack widths for all specimens were within w_m=0.20-0.35, indicating that the 20 elastic cycles produced some

degradation at the concrete-rebar interface and increased the crack widths. Apart from C0-16C that failed due to buckling at the free rebar region, all w_m-ε curves show an increase in w_m with the increase in the number of inelastic cycles. At the first set of inelastic cycles ($2\times\varepsilon_y$) the increase in w_m was only around 0.01 mm, yet at the second set ($2\times\varepsilon_y$) the increase in w_m was between 0.1 mm (for CS-20C) and 0.7 mm (for C0-20C). As observed from Figure 13c,d, cyclic loading seems to have a more detrimental effect on the non-spliced members in comparison to those with mechanical splices.

3.2.3 Crack spacing

The crack spacing is dictated by a transfer length ($l_t=s_{r0}$) that can be defined as a length necessary to reach the concrete cracking stress in the cross-section. From strain compatibility, the minimum crack spacing (s_{rmin}) gives the closest point to an existing crack at which another crack can be formed, whilst the maximum crack spacing is considered as $s_{rmax} = 2\times s_{rmin}$ [42-43]. In practice, the concept of average crack spacing s_{rm} is also used for estimating average crack widths w_m, where s_{rm} can be expressed in terms of s_{rmin}/s_{rm} =0.6-0.7 or s_{rmax}/s_{rm} = 1.33–1.50 [43-46]. The average crack widths w_m is obtained by multiplying the average crack spacing by the difference between the average steel strain ε_{sm} and the average residual strain in the concrete between the cracks ε_{cm}.

Table 4 gives the experimentally-obtained s_{rmin}, s_{rmax} and s_{rm} crack spacings corresponding to rebar yield and ultimate, considering both newly initiated cracks and fully developed cracks. Although in terms of s_{rmin} and s_{rmax}, there is a scatter depending on the number of cracks n_{cr}, without a clear influence from the presence of the coupler, s_{rm} at yield seems to be around 200 mm, except for CC-16C. At t ultimate s_{rm} is in the range of 100-150 mm. More importantly, at yield, s_{rmin}/s_{rm} and s_{rmax}/s_{rm} ratios show very similar values for all tested configurations with average s_{rmin}/s_{rm}=0.58-0.66 and s_{rmax}/s_{rm}=1.27-1.30 for each splice type. These are in good agreement with observations reported in previous studies [e.g. 43, 47]. At ultimate, as the n_{cr} increases, both s_{rmin} and s_{rmax} vary, with an average s_{rmin}/s_{rm}=0.47-0.50 and s_{rmax}/s_{rm}=1.58-1.86. From Table 4, combined with observations from analysis of crack kinematics, the presence of the coupler in these cases does not appear to have a notable effect on the member response around rebar yield, with some influence appearing towards ultimate.

3.2.4 Bond distributions

Nonlinear numerical procedures were used to assess the reinforcement stresses and concrete-rebar slip distributions along the length of the in-concrete members. The 3D finite element models, constructed within ABAQUS [48], adopt 8-noded brick elements (C3D8R) for concrete and steel rebar elements. The couplers were modelled as single 3D cylindrical blocks without accounting for the threaded connection itself, as the results from the elastic slip tests (e.g. Figure 8) indicated low strain levels at the threads. The couplers were connected to rebars through a tie constraint. The 'concrete damage plasticity' model (CDP) was employed using the following constitutive parameters: bi-axial behaviour of concrete f_{b0}/f_c=1.16, factor for the shape of the deviatoric plane K_c=2/3, dilation angle φ=40°, and surface eccentricity ϵ=0.1, as described in detail elsewhere [49].

The compressive stress-strain relationship followed the representation obtained from Ø100×200 mm cylinder compression tests, considering the values given in Section 2.1. In tension, a bi-linear tension softening law, extracted from a nonlinear model by converting the crack width to strain as a function of the characteristic element length l_{ch}, was considered. The steel materials were modelled through a bi-linear representation with hardening using the material strengths obtained from the coupon steel tests. The interaction between steel and concrete was modelled using a complete bond-slip representation considering good bond conditions with bond coefficients γ_b>4.0 [35]. As illustrated in Figures 14a-c, the validation studies showed good agreement in terms of crack initiation and kinematics, crack patterns and load-strain F-ε curves considering the rebar-concrete bonded length, particularly since detailed tension stiffening and bond-slip representations were considered [50].

Figure 14d-f illustrate the steel stress and concrete-rebar slip distributions for three configurations investigated at rebar yield, as well as the numerical crack patterns that resemble those obtained in the tests (Figure 12). For the non-spliced member, the rebar stresses are nearly uniform throughout its length with the highest values at the free rebar region. In contrast, for spliced cases, lower stresses around $0.5\times f_y$ are obtained at the coupler, whilst yield is also reached outside the concrete body. These distributions show that, for such configurations, reinforcement fracture is likely to occur in the free rebar region, as obtained in the experimental results. As the coupler has a larger diameter than the rebar, the stresses within that region are consistently lower than at the rebar. More importantly, the concrete-rebar slip curves in Figures 14a,b,c show distinct distributions and slip values as a function of the coupler length, showing that larger slip values occur with the increase in coupler length.

For the slender coupler cases, differences in bond capacity at the coupler compared to the rebar region shift the subsequent crack location to outside the coupler and rebar-coupler interface, initially towards the concrete/rebar region, and ultimately to the free rebar region where failure occurs. As for the in-air tests, the ratio between these lengths may influence considerably the performance of in-concrete

members with couplers. These effects may become less significant with the increase in total specimen length as the ratio between the length of the embedded rebar and embedded coupler regions increases.

4. Comparative assessments

This section examines the elastic and inelastic load-strain response of the investigated configurations, as well as the cracking characteristics in the concrete members. Comparative assessments are carried out considering the main behavioural stages with emphasis on the post-cracking and post-yielding regimes. The stages prior to steel yielding are particularly important for serviceability and durability requirements as well as for force transfer purposes, whilst the post-yield stages are of direct relevance for the assessment of ductility.

4.1 Cracking characteristics

Crack patterns and widths are primarily dependent on the reinforcement ratio, without a significant influence from the concrete material properties [22,43]. For tension members, the rebar surface characteristics, bar diameter and concrete cover, also affect the cracking behaviour. Couplers have higher diameter than the connected rebars, whilst their surface is typically regular and plain in comparison with the deformed surface of the rebar. For relatively large couplers, the local reinforcement ratio at the coupler section $\rho_{s,co}$ in conjunction with its bond characteristics $\tau_{b,co}$, in comparison with the actual reinforcement ratio $\rho_{s,b}$ at the rebar section combined with its surface type $\tau_{b,}$ have a direct effect on the crack spacing and kinematics. A comparative study on the influence of the size factor $\lambda_s=d_cL_c/(d_bL_b)$ on the crack spacing ratio λ_{co} is presented below by considering a range of coupler configurations, with the relevant details extracted from available data sheets [28,29,51-60]. The coupler and rebar geometries were used to assess $\rho_{s,b,}$ $\rho_{s,co}$ and the crack spacing ratio $\lambda_{co}=s_{r0,b/}s_{r0,co}$ in which $s_{r0,b}$ is the crack spacing at the rebar region, while $s_{r0,co}$ represents the crack spacing at the coupler region. The couplers are idealised as cylindrical steel elements with regular/plain surfaces and without slip at the connections to the rebars.

For comparison purposes, the crack spacing $s_{r0,i}$ (Equation 1) is considered to correspond to s_{rmin} being equal to the transfer length through bond. For the assessments presented in Figure 15, γ_b=2.5 for good bond characteristics is assumed [61], as suggested in existing guidelines [45,46]. Consequently, the bond capacity at the coupler with regular surface $\tau_{b,co}$ is 40% of a corresponding deformed element [46] (Equation 2). Considering the above limits in terms of bond capacity at rebars and at couplers, $s_{r0,b}$ and $s_{r0,co}$ may be determined from Equations (3a,b), whilst the λ_{co} ratio can be obtained from Equation (4) as a function of the member, coupler and rebar section sizes only.

Figure 15 depicts the relationship between the size factor λ_S and crack spacing ratio λ_{co}. Values of $\lambda_s \leq 1.0$ represent relatively compact couplers, whilst $\lambda_s > 1.0$ are more slender. On the other hand, values $\lambda_{co} \leq 1.0$ indicate narrower crack spacings that occur at the rebar region in comparison to the coupler region, whilst $\lambda_{co} > 1.0$ signify geometries and bond characteristics that produce wider cracks at the rebar region in comparison to the coupler region. Narrower crack spacings produce a more uniform stress distribution throughout the member length, whilst wider crack spacings generate less cracks that produce strain localisation and more rapid development of plasticity [50]. As failure outside the coupler region is desirable in practice, narrower cracks need to develop at the rebar region ($\lambda_{co} \leq 1.0$). As observed from Figure 15, compact couplers with size factors below and around $\lambda_S \leq 1.0$ tend to exhibit $\lambda_{co} \leq 1.0$, hence favouring the development narrower crack spacings at the rebar region. In contrast, relatively slender couplers are expected to have $\lambda_{co} > 1.0$, with a more significant influence on the cracking response.

$$s_{r0,i} = \frac{d_i f_{ct}}{4\tau_b \rho_{s,i}} \text{ where } i=b \text{ for rebar, and } co \text{ for coupler} \quad (1)$$

where $\rho_{s,b} = A_s / A_c$ and $\rho_{s,co} = A_{co} / A_c$

$$\tau_{b,co} = 0.4\tau_b \quad (2)$$

where $\tau_b = \gamma_b \sqrt{f_c}$ and γ_b=2.5

$$s_{r0,b} = \frac{d_b f_{ct}}{4\tau_b \rho_{s,b}} \text{ and } s_{r0,co} = \frac{d_{co} f_{ct}}{1.6\tau_b \rho_{s,co}} \quad (3)$$

$$\lambda_{co} = \frac{s_{r0,b}}{s_{r0,co}} = 0.4 \frac{d_b \rho_{s,co}}{d_{co} \rho_{s,b}} \quad (4)$$

Figure 16 shows a qualitative comparison between the tension damage (crack) patterns at rebar yield for members incorporating three types of splices (UHC, SWC, GSC [49,50,53]) and the corresponding non-spliced models, resulting from nonlinear numerical simulations using the procedures described in Section 3.2.4. It can be observed that for 16 mm rebars with UHC-16 ($\lambda_S \approx 1.0$), the cracks are similar to the non-spliced member (NON-16), whilst for SWC-16 (also with $\lambda_S \approx 1.0$), the cracks are outside the coupler region. It is shown that for such λ_S ranges, couplers do not have a notable influence on the cracking response, as also observed from the tests described above. For GSC-16 with $\lambda_S > 2.0$, cracks occur at the coupler. For exaggerated coupler geometries with respect to member size (UHC-32, SWC-32, GSC-32) and very high reinforcement ratios, analysed herein for comparison reasons, cracks occur at the coupler in all cases. These observations, in conjunction with the damage pattern for GSC-16, suggest a behaviour similar to the results shown in Figure 15 in terms of the influence of the coupler geometry on the crack spacing.

4.2 Load-strain response

In the stabilised cracking stage, the stiffness of the RC member is in between the stiffness of the elastic element and of the fully cracked element. This tension stiffening effect is expressed analytically as a reduction in the mean steel stress in relationship to the bare steel bar. After cracking initiates, the tension stiffening decreases gradually until steel strains concentrate at cracked sections, and fully disappears at yielding when the response is controlled by steel bar only. A detailed comparative assessment in terms of stiffness and capacity between experimental and predicted curves is illustrated in Figure 17.

A gauge length of 590 mm over the concrete element was considered to assesses ε for the in-concrete members, whilst a gauge length of L_c+4d_b for the in-air specimens, respectively. The predicted F-ε curves using Equations (6-8) were derived using the test material strengths and Eurocode 2 guidelines and considering β_t=0.7, σ_{sr}=1.3, ρ_l=1.78%, E_s=200000 and E_{sh}=800 MPa [45,46,61].

$$\varepsilon_{s,m} = \varepsilon_{s1} \rightarrow \sigma < \sigma_s \leq \sigma_{sr1} \tag{5}$$

$$\varepsilon_{s,m} = \varepsilon_{s2} - \frac{\beta_t\left(\sigma_s - \sigma_{sr1}\right) + \left(\sigma_{srn} - \sigma_s\right)}{\sigma_{srn} - \sigma_{sr1}}\left(\varepsilon_{sr2} - \varepsilon_{sr1}\right) \rightarrow \sigma_{sr1} < \sigma_s \leq \sigma_{srn} \tag{6}$$

$$\varepsilon_{s,m} = \varepsilon_{s2} - \beta_t\left(\varepsilon_{sr2} - \varepsilon_{sr1}\right) \rightarrow \sigma_{srn} < \sigma_s \leq f_y \tag{7}$$

$$\varepsilon_{s,m} = \varepsilon_{sy} - \beta_t\left(\varepsilon_{sr2} - \varepsilon_{sr1}\right) + \left(f_y / f_u\right)\left(1 - \sigma_{sr1} / f_y\right)\left(\varepsilon_{s2} - \varepsilon_{sy}\right) \rightarrow f_y < \sigma_s \leq f_u \tag{8}$$

As illustrated in Figures 17a-c, the predicted curves show good agreement with the test results for all monotonic tests in terms of stiffness and yield load. A slightly different response is obtained for the members provided with compact couplers, as the steel material in the rebars had a rounded elasto-plastic curve around the yield, having a direct implication on the F-ε response of the in-concrete counterparts (CC-16M and CC-20M, respectively). Also, the experimental-to-predicted curves comparison indicate some influence from the coupler geometry to the stiffness. Figures 17d-f show that the cyclic tests F-ε curves are nearly inscribed within the monotonic curves and in close agreement with the predicted F-ε curves up to ε=0.5%. It is worth noting that the 20×cycles applied in the elastic regime of the rebar had a minimal effect on the deformation of the non-spliced C0-20C, yet it is indicated that for CC-20C and CS-20C, residual strains were accumulated before yielding. This suggests that the presence of the coupler, with its regular surface, allowed some bond degradation within the elastic cycles.

As discussed in Section 4.1 and above, the coupler size has an influence on the crack kinematics and since it affects the member stiffness as, particularly for the members with slender couplers, the stiff-

ness deviates from that of the non-spliced member. To further investigate this aspect, Figure 18 illustrates the F-ε responses of the concrete body for the numerical models described in Section 4.1, with the crack patterns shown in Figure 15. As observed in Figure 18, there is a clear increasing trend in terms of cracked stiffness with respect to the coupler size. Both SWC-16 and UHC-16 (with $\lambda_s \approx 1.0$) are within the same ranges, whilst GSC-16 (with $\lambda_s > 2.0$) has the stiffest response. To capture the reduction in stiffness with the increase in coupler size factor (λ_s), a cracked stiffness reduction factor β_E, depicted by Equation (9) is suggested, and compared with the results in Figure 19.

$$\beta_E = 1 - 0.25\lambda_s \tag{9}$$

Figure 20 shows a comparison between the test or numerical F-ε responses of the concrete members and the corresponding predicted curves using Equations (5-8) for non-spliced members which were further modified using the β_E estimated from Equation (9) for members incorporating couplers. As observed, the predicted curves are in good agreements for all the cases investigated, with both compact ($\lambda_s \leq 1.0$) and slender couplers ($\lambda_s > 1.0$).

4.3 Ductility and energy dissipation

For comparison purposes, the cumulative energy dissipation of the test members subjected to cyclic loading is estimated from the F-ε behaviour shown in Figures 9 and 11 as the enclosed areas from the entire curve considering the key characteristic strain levels. Figures 21a,b illustrate the energy dissipation at yield ε_y, before the first inelastic cycle at ($2\times\varepsilon_y$), after completing four cycles at ($2\times\varepsilon_y$), before the first inelastic cycle at ($5\times\varepsilon_y$), after completing four cycles at ($5\times\varepsilon_y$), at ultimate ε_u, and at fracture ε_f, for the in-air members. Figures 21c,d illustrate the energy dissipation for the concrete members, considering the same ε levels described above, and the energy dissipated before the first elastic cycle. It is worth noting that for the concrete members the energy dissipated through the 20 elastic cycles is included in the values given at yield ε_y. In each plot in Figure 21, a bar chart with the energy dissipated through the four cycles at $5\times\varepsilon_y$ is also reported.

As observed from Figure 21, for all members, the level of energy dissipated within the elastic regime of the reinforcement is within similar ranges. The energy dissipation curves show nearly identical responses, irrespective of the presence of coupler, up to inelastic cycles of $2\times\varepsilon_y$. As the strain level increases to $5\times\varepsilon_y$, a distinctive difference is observed, which can be grouped according to the coupler geometry. As illustrated in the charts plotted in the top-left corner of each plot in Figure 21 for all cycles at $5\times\varepsilon_y$, the highest energy dissipation was recorded by the non-spliced members in all cases, followed by those with compact couplers and then those with slender couplers. This trend is further maintained for the energy dissipated at ultimate ε_u and at fracture ε_f in all cases. It is worth noting,

that a close inspection of the F-ε curves for the inelastic cycles indicated that there was no pinching effect at the transition between tension-compression loading for the concrete members.

A comparative assessment in terms of ductility is performed by considering the ratio between ultimate-to-yield strain $\varepsilon_u/\varepsilon_y$ given in Tables 2 and 3, in which ε_u corresponds to the maximum strength. The ratios illustrated in Figure 22 show consistent reduction between the in-concrete and in-air specimens for both monotonic and cyclic tests. For the monotonic tests the reduction ratios between in-concrete to in-air ductility ratios are 12.5% for non-spliced members, 17% for those with compact couplers, and 24% for those with slender couplers. For the cyclic tests, the reduction of in-air to in-concrete ductility ratios is 20% for the non-spliced members, 18% for those with compact couplers, and 12.3% for those with slender couplers. A decreasing trend is also observed in terms of reduction in ductility ratios considering the member type. These reductions are between 24-28% for in-concrete tests and 18-31% for in-air tests from the reference non-spliced configuration, depending on the type of coupler and loading.

For the application of mechanical splices in dissipative zones according to Eurocode 8 [27], the behaviour should be validated by testing under conditions compatible with the selected ductility class (i.e. medium ductility: DCM, or high ductility: DCH), which is directly related to the material ductility classes stipulated in Eurocode 2 [61]. For DCM, reinforcement Classes B and C are allowed in dissipative zones, whilst for DCH only Class C reinforcement is permitted in dissipative zones. Although the level of ultimate strain decreased in some cases for coupled splices compared with the non-spliced specimens, the test results show that the minimum criterion for Class C reinforcement (i.e. ε_u>7.5%) in Eurocode 2 was generally met. Accordingly, most of these coupled bars satisfy the strain requirements for reinforcement in seismic design according to Eurocode 8 for DCH.

5. Concluding remarks

This paper described an experimental programme carried out on in-air and in-concrete mechanical splices incorporating two types of threaded couplers subjected to uniaxial monotonic and cyclic loading. Complementary numerical studies using nonlinear finite element procedures were undertaken and the validations against the concrete members tested enabled supplementary parametric investigations to be carried out. The tests showed that both types of couplers had marginally higher strains than the non-spliced reference bar within the elastic cyclic test, without notable slip at the threads. It was also indicated that slender splices provide lower ductility than splices with compact couplers as well as non-spliced specimens with reductions up to 35%. Both coupler types however developed ultimate strains around or above 7.5%, suggesting that they generally comply with requirements for high ductility reinforcement according to European codes.

Cyclic loading also had a detrimental effect on the in-air response with reductions up to 25% in the strain at fracture in comparison to the monotonic cases, whilst no pinching effect was observed at the tension-compression loading transition for the concrete members. The detailed strain measurements showed that the enlarged rebar cross-section near the threads of compact couplers shifts the weak area away from the coupler region, whilst for the slender couplers some strain localisation occurs at the threads prior to rebar yield and at the coupler-to-rebar interface. For both the in-air and in-concrete behaviour, the ratios between coupler-to-rebar lengths influences the response in members with longer couplers producing more rapid straining of the rebar and earlier failure. The analysis of the experimental crack widths showed values below 0.1 mm for monotonic tests and up to 0.35 mm for cyclic tests within the elastic range of the rebar, suggesting that the elastic cycles produced some degradation at the concrete-rebar interface. It was indicated that the presence of the coupler had minimal or no effect in terms of crack spacing up to rebar yield. Also, compact couplers with size factors below and around 1.0 tend to favour the development narrower crack spacings at the rebar region producing a more desirable uniform stress distribution throughout the rebar length.

The numerical results showed that for the in-concrete splices, lower stresses of around $0.5 \times f_y$ are obtained at the coupler, whilst for the non-spliced configurations the rebar stresses are nearly uniform throughout their length. More importantly, the concrete-rebar slip curves show distinct distributions and slip values as a function of coupler length, indicating larger slip with the increase in coupler length, primarily due to the regular surface compared to the deformed surface of the rebar. Key observations showed that the increase in coupler size reduces the cracked stiffness of the member. This aspect may be captured through a stiffness reduction factor, as a function of the suggested coupler size factor, which may be employed in existing models for an effective assessment of the load-strain response of embedded mechanical splices.

Acknowledgements

Funding from the Research Award Scheme of the Institution of Structural Engineers in the UK for part of the work described in this paper is gratefully acknowledged. The authors would like to thank the technical staff of the Structures Laboratories at Imperial College London, for their assistance with the experimental work. The support of Dextra Manufacturing through the provision of materials is also gratefully acknowledged.

References

[1] Bennett EW. Fatigue tests of spliced reinforcement in concrete beams. ACI Special Publication 75. 1982 Sep 1;75:177-94.

[2] Sritharan S, Ingham J, Priestley M, Seible F. Design and Performance of Bridge Cap Beam/Column Using Headed Reinforcement and Mechanical Couplers. ACI Special Publication 184. 1999 Nov 1; 184:7-22

[3] Ingham JM, Bai AS. Seismic performance of mechanically coupled reinforcing bars. Magazine of Concrete Research. 2009 Sep;61(7):529-37 https://doi.org/DOI 10.1680/macr.2008.00098

[4] Hegger J, Roeser W, Lotze D. Kurze Verankerungslängen mit Rechteckankern. Beton-und Stahlbetonbau. 2004 Jan 1;99(1):1-9.

[5] Hulshizer AJ, Ucciferro JJ, Gray GE. Mechanical Reinforcement Couplings Meet Demands of Strength and Constructibility. Concrete International. 1994 Dec 1;16(12):47-52.

[6] Tazarv M, Saiid Saiidi M. Low-damage precast columns for accelerated bridge construction in high seismic zones. ASCE Journal of Bridge Engineering. 2015 Sep 25;21(3):04015056. https://doi.org/10.1126/science.1186253

[7] Aaleti S, Brueggen BL, Johnson B, French CE, Sritharan S. Cyclic response of reinforced concrete walls with different anchorage details: experimental investigation. Journal of Structural Engineering. 2012 Sep 13;139(7):1181-91. https://doi.org/10.1061/(ASCE)ST.1943-541X.0000732

[8] Lee SJ, Lee DH, Kim KS, Oh JY, Park MK, Yang IS. Seismic performances of RC columns reinforced with screw ribbed reinforcements connected by mechanical splice. Computers and Concrete. 2013;12(2):131-49. https://doi.org/10.12989/cac.2013.12.2.131

[9] ISO 15835-1:2009, steels for the reinforcement of concrete - reinforcement couplers for mechanical splices of bars - part 1: requirements. Geneva: ISO; 2009.

[10] ASTM International - ASTM A1034 / A1034M - 10a - Standard Test Methods for Testing Mechanical Splices for Steel Reinforcing Bars, West Conshohocken, PA 19428-2959. United States, 2015

[11] Rowell SP, Grey CE, Woodson SC, Hager KP. High strain-rate testing of mechanical couplers. U.S. Army Engineer Research and Development Center, Technical Report ERDC TR-09-8; Port Hueneme, CA, September 2009.

[12] Noureddine I. Plastic energy absorption capacity of #18 reinforcing bar splices under monotonic loading MSc Thesis. Sacramento: California State University; 1996. p. 108.

[13] Paulson C, Hanson JM. Fatigue Behavior of Welded and Mechanical Splices in Reinforcing Steel. NCHRP Report. 1991 Dec:10-35

[14] Haber ZB, Saiidi MS, Sanders DH. Behavior and simplified modeling of mechanical reinforcing bar splices. ACI Structural Journal. 2015 Mar 1;112(2):179. https://doi.org/10.14359/51687455

[15] McCabe SL. Mechanical coupler testing report, Test report, University of Kansas Structural Engineering and Materials Laboratory, 1994

[16] Tazarv M, Saiidi MS. Seismic design of bridge columns incorporating mechanical bar splices in plastic hinge regions. Engineering Structures. 2016 Oct 1;124:507-20. https://doi.org/10.1016/j.engstruct.2016.06.041

[17] Alam MS, Youssef MA, Nehdi ML. Exploratory investigation on mechanical anchors for connecting SMA bars to steel or FRP bars. Materials and structures. 2010 Dec 1;43(1):91-107. https://doi.org/10.1617/s11527-010-9601-0

[18] Coogler KL, Harries KA, Gallick M. Experimental study of offset mechanical lap splice behavior. ACI Structural Journal. 2008 Jul 1;105(4):478.

[19] Ameli MJ, Parks JE, Brown DN, Pantelides CP. Seismic evaluation of grouted splice sleeve connections for reinforced precast concrete column-to-cap beam joints in accelerated bridge construction. PCI Journal. 2015 Mar 1;60(2):80-103. https://doi.org/10.15554/pcij.03012015.80.103

[20] Haber ZB, Saiidi MS, Sanders DH. Seismic performance of precast columns with mechanically spliced column-footing connections. ACI Structural Journal. 2014 May 1;111(3):639. https://doi.org/10.14359/51686624

[21] Parks JE, Brown DN, Ameli MJ, Pantelides CP. Seismic Repair of Severely Damaged Precast Reinforced Concrete Bridge Columns Connected with Grouted Splice Sleeves. ACI Structural Journal. 2016 May 1;113(3):615. https://doi.org/10.14359/51688756

[22] Lorrain M, Maurel O, Seffo M. Cracking behavior of reinforced high-strength concrete tension ties. ACI Structural Journal. 1998 Sep 1;95(5):626-35.

[23] Scott RH, Gill PA. Short-term distributions of strain and bond stress along tension reinforcement. The Structural Engineer. 1987 Jun;65(2):39-43. https://doi.org/10.4172/scientificreports.226

[24] Goto Y. Cracks formed in concrete around deformed tension bars. ACI Journal, 1971 68(4), 244–251. https://doi.org/10.14359/11325

[25] Kankam CK. Relationship of bond stress, steel stress, and slip in reinforced concrete. Journal of structural engineering. 1997 Jan;123(1):79-85. https://doi.org/10.1061/(ASCE)0733-9445(1997)123:1(79)

[26] Bompa DV, Elghazouli AY. Ductility considerations for mechanical reinforcement couplers. Structures 2017 Nov 1;12:115-119 https://doi.org/10.1016/j.istruc.2017.08.007

[27] Eurocode 8: Design of structures for earthquake resistance Part 1: general rules, seismic actions and rules for buildings. CEN, Brussels (Belgium), 2005.

[28] PTSC (Cold forged sleeve with parallel threaded coupler) Dextra Group – Griptec https://www.dextragroup.com/activities/technical-solutions-for-construction/solutions/25-griptec, accessed 11 Apr 2018

[29] PTC (Parallel threaded coupler) Dextra Group - Fortec/Bartec https://www.dextragroup.com/activities/technical-solutions-for-construction/solutions/24-concrete-construction/rebar-splicing/50-fortec, accessed 11 Apr 2018

[30] Balazs GL. Cracking analysis based on slip and bond stresses. ACI materials journal. 1993 Jul 1;90:340-348

[31] Schenkel M. On bond behavior of reinforcing bars with limited cover" (in German, "Zum Verbundverhalten von Bewehrung bei kleiner Betondeckung"), ETHZ, Swiss Federal Institute of Technology Zürich, Report No. 237, Birkhäuser, Basel-Boston-Berlin, Switzerland, 162 p. 1998

[32] CEN (European Committee for Standardization) ISO 15630-1:2010 Steel for the reinforcement and prestressing of concrete – Test methods - Part 1: Reinforcing bars, wire rod and wire. CEN, Brussels (Belgium), 2010

[33] Elghazouli AY, Bompa DV, Xu B, Stafford PJ, Ruiz-Teran AM. Inelastic behaviour of RC members incorporating high deformability concrete. In High Tech Concrete: Where Technology and Engineering Meet 2018 (pp. 2399-2406). Springer International Publishing. https://doi.org/10.1007/978-3-319-59471-2_273

[34] Elghazouli AY, Bompa DV, Xu B, Stafford PJ, Ruiz-Teran AM Performance of rubberised reinforced concrete members under cyclic loading Engineering Structures 2018 166:526–545 https://doi.org/10.1016/j.engstruct.2018.03.090

[35] Bompa DV, Elghazouli AY. Bond-slip response of deformed bars in rubberised concrete. Construction and Building Materials. 2017 Nov 15;154:884-98. https://doi.org/10.1016/j.conbuildmat.2017.08.016

[36] CEN (European Committee for Standardization) (EN 206-1:2000 Concrete — Part 1: specification, performance, production and conformity. CEN, Brussels (Belgium), 2000.

[37] ISO 15835-1:2018, steels for the reinforcement of concrete - reinforcement couplers for mechanical splices of bars - part 1: requirements. Geneva: ISO; 2018.

[38] Xu B, Bompa DV, Elghazouli AY, Ruiz-Teran AM, Stafford PJ. Behaviour of rubberised concrete members in asymmetric shear tests. Construction and Building Materials. 2018 Jan 20;159:361-75. https://doi.org/10.1016/j.conbuildmat.2017.10.091

[39] LaVision - DaVis digital image correlation software http://www.lavision.de/en/products/davis-software/index.php, accessed 11 Apr 2018

[40] Bompa DV, Elghazouli, AY. Inelastic cyclic behaviour of RC members incorporating threaded reinforcement couplers, Engineering Structures 2019, under review

[41] Tassi, G. and Magyari, B., 1982. Fatigue of reinforcements with pressed sleeve splices. International Assoc. for Bridge and Structural Engineering, pp.265-271.

[42] Borosnyói A, Balázs GL. Models for flexural cracking in concrete: the state of the art. Structural Concrete. 2005 Jun;6(2):53-62. https://doi.org/10.1680/stco.2005.6.2.53

[43] Rizkalla SH, Hwang L. Crack prediction for members in uniaxial tension. ACI Journal Proceedings 1984 Nov 1 *81*(6), 572–579.

[44] Beeby AW. The prediction of crack widths in hardened concrete. The Structural Engineer. 1979 Jan 1;57(1):9-17. https://doi.org/10.1046/j.1365-2168.1998.00824.x

[45] CEB-FIP. CEB-FIP Model Code 1990: Design Code. Thomas Telford; 1993.

[46] fib – Fédération internationale du béton. Model Code 2010 – final draft, vol. 1 & vol. 2, fib Bulletins 65 & 66, Lausanne (Switzerland); 2012.

[47] Bigaj AJ. Structural dependence of rotations capacity of plastic hinges in RC beams and slobs (Doctoral dissertation, TU Delft, Delft University of Technology).

[48] DSS (Dassault Systèmes Simulia Corp.) (2010) Abaqus Analysis Users‘ Manual, Version 6.10. DSS, Providence, RI, USA.

[49] Bompa DV, Elghazouli AY. Numerical modelling and parametric assessment of hybrid flat slabs with steel shear heads. Engineering Structures. 2017;142, 67–83 https://doi.org/10.1016/j.engstruct.2017.03.070

[50] Bompa DV, Elghazouli AY. Ductility of reinforced concrete members incorporating mechanical splices, In proceedings of 16th European Conference on Earthquake Engineering (16ECEE), ID 11604, Thessaloniki, Greece, June 18-21 2018.

[51] TTSC (Cold forged sleeve with taper threaded coupeler) BarSplice Products - Grip-twist data sheet http://www.barsplice.com/Brochures/current/TTGT_DataSheet.pdf, accessed 11 Apr 2018

[52] TTC (Taper threaded coupler) LENTON Standard Couplers - A12 https://www.erico.com/category.asp?category=R2017, accessed 11 Apr 2018

[53] MFC (Metal filled coupler) Erico Cadweld - Rebar Metal Filled Mechanical Splices - https://www.erico.com/catalog/literature/C482B-WWEN.pdf , accessed 11 Apr 2018

[54] SWC (Swaged coupler) BarSplice Bargrip data sheet http://www.barsplice.com/Brochures/BarGrip_DataSheet_metric_RevJ.pdf, accessed 11 Apr 2018

[55] UHC (Upset headed coupler) Headed Reinforcement Corp. - HRC 500 Series http://www.hrc-usa.com/hrc-500-series/, accessed 11 Apr 2018

[56] OSWG (Offset wedge swaged coupler) – Lenton Quick wedge mechanical lap splicing system https://www.erico.com/category.asp?category=R1432, accessed 11 Apr 2018

[57] BLC (Bolt lock coupler) and OBLC (Offset bolt lock couplers) BarSplice Zap Screwlock data sheet http://www.barsplice.com/Brochures/current/Zap_DataSheet.pdf, accessed 11 Apr 2018

[58] GSC (Grouted sleeve coupler) – Splice Sleeve North America - NMB Splice http://www.splicesleeve.com/dimensions.html, accessed 11 Apr 2018

[59] TTC-GSC (Taper threaded-Grouted sleeve coupler) Interlock grout-filled precast splicing system https://www.erico.com/category.asp?category=R2049, accessed 11 Apr 2018

[60] Sabău M, Pop I, Oneţ T. Experimental study on local bond stress-slip relationship in self-compacting concrete. Materials and Structures. 2016 Sep 1;49(9):3693-711. https://doi.org/10.1617/s11527-015-0749-5

[61] Eurocode 2: Design of Concrete Structures, Part 1–1: General Rules for Buildings, CEN, Brussels (Belgium), 2004.

List of tables

Table 1 Details of test specimens
Table 2 Test results of uniaxial in-air rebar tests
Table 3 Test results of concrete members
Table 4 Crack spacing

List of figures

Figure 1 a) Coupler systems: (Threaded: PTC Parallel threaded, TTC Taper threaded, PTSC Cold forged sleeve with parallel threads, TTSC Cold forged sleeve with taper threads, TTWC Taper threads from welded heads), (Swaged: SWC Swaged, OSWC Offset wedge swaged, BLC Bolt lock, OBLC Offset bolt lock), (Grouted: GSC Grouted sleeve, TTC/GSC Taper threaded-Grouted sleeve), (Other systems: UHC Upset headed, MFC Metal filled, RTC Rib thread);
Figure 2 a) ductility criteria; b) average size factor λ_s
Figure 3 Uniaxial in-air sample configurations for PTC and PTSC couplers with 16mm and 20mm rebars
Figure 4 In-concrete specimens: a) with PTC, b) with PTSC, c) cross-sections through members
Figure 5 Reinforcement bar details
Figure 6 Schematic representation of the loading procedures ISO 15835-2:2009 [9]: a) S2 inelastic cyclic, b) S1 elastic cyclic
Figure 7 Testing machine with: a) in-air sample, b) in-concrete specimen
Figure 8 Elastic slip results
Figure 9 σ-ε relationships for in-air tests: a) 16 mm monotonic, b) 16 mm cyclic, c) 20 mm monotonic, d) 20 mm cyclic
Figure 10 Longitudinal strains at yield, half ultimate and ultimate applied deformation for a) AC-16C, b) AS-16C; c) failure location of investigated cyclic specimens
Figure 11 F - ε response for in-concrete members provided with 20 mm bars a) monotonic tests, b) cyclic tests.
Figure 12 Crack pattern and crack widths for in-concrete members provided with 20 mm bars: monotonic tests a) C0-20M, b) CC-20M, c) CS-20M; cyclic tests d) C0-20C, e) CC-20C, f) CS-20C
Figure 13 a) Average crack width w_m vs reinforcement stress σ_{sm}, b) average crack width w_m vs member mean strain ε for in-concrete monotonic tests; c,d) average crack width w_m vs member mean strain ε for in-concrete cyclic tests
Figure 14 Numerical validation of F-ε responses for: a) C0-20M, b) CC-20M, c) CS-20M; Steel stress σ_{sm} and slip s distributions for in-concrete models at yield for: d) non-spliced model C0-20M, e) CC-20M with compact coupler, f) CS-20M with slender coupler
Figure 15 Relationship between slenderness ratio λ_s and crack spacing ratio λ_{co}
Figure 16 Crack patterns for 16 mm and 32 mm non-spliced models and models incorporating splices with UHC, SWC, GSC
Figure 17 Test and predicted F-ε responses for monotonic in-air and in-concrete members incorporating 16 mm and 20 mm rebars: a) non-spliced specimens, b) with compact couplers, c) with slender couplers; cyclic in-concrete members incorporating 20 mm rebars for member: d) without couplers, d) with compact couplers, e) with slender couplers
Figure 18 F-ε for 16 mm non-spliced models and models with UHC, SWC and GSC
Figure 19 Relationship between stiffness reduction factor β_E and size factor λ_s
Figure 20 Predictions of F-ε response by considering cracked stiffness reduction factor β_E
Figure 21 Energy dissipation for in-air specimens a) 16 mm, b) 20 mm; in-concrete specimens c) 16 mm, d) 20 mm
Figure 22 Ductility comparisons for: a) monotonic tests, b) cyclic tests

Nomenclature

Greek letters

β_E - cracked stiffness reduction factor
β_t – tension stiffening factor
γ_b - bond coefficient
ε – mean strain
ε_f – mean strain at fracture
ε_y – mean strain at yield
ε_u - ultimate strain/strain at peak load
$\varepsilon_{s,m}$ - mean steel strain
ε_{s1} - rebar strain in the uncracked concrete
ε_{s2} - rebar strain at the crack
ε_{sy} - the steel yield strain
φ - dilation angle
λ_{co} - crack spacing ratio
λ_s - size/bulkiness parameter
μ_ε – mean strain ductility ratio
ρ_l - reinforcement ratio
$\rho_{s,co}$ - reinforcement ratio at the coupler section
$\rho_{s,b}$ - reinforcement ratio at rebar section
σ – stress
σ_s – steel stresses at crack
σ_{sm} - average reinforcement stress
σ_{sr} - reinforcement stress factor
σ_{sr1} is the steel stress at crack initiation
σ_{srn} is the steel stress at crack stabilisation
$\tau_{b,co}$ - bond characteristics at coupler
τ_b - bond characteristics at rebar
ϵ - surface eccentricity
Δ – applied displacement
Δ_y - yield displacement

Lowercase latin letters

d_b – rebar diameter
d_c – coupler length
f_{b0}/f_c - bi-axial to uniaxial concrete strength
f_c – cylinder compressive strength
$f_{c,cube}$ – cube concrete strength
f_{ct} - tensile strength of concrete
$f_{ct,sp}$ – concrete splitting strength
f_y - yield strength
f_u - ultimate strength
$f_{y,b}$ – yield strength of the rebar
$f_{u,b}$ - ultimate strength of the rebar
$f_{u,sp}$ – ultimate capacity of the splice
l_{ch} - characteristic element length
l_s - clear length
l_t - transfer length
n_{cr} – number of cracks
s - slip
s_{r0} – reference crack spacing
$s_{r0,b}$ - crack spacing at the rebar
$s_{r0,co}$ - crack spacing at the coupler
s_{rmin} - minimum crack spacing
s_{rmax} - maximum crack spacing
w_m - average crack widths
w_{max} – maximum crack width

Uppercase latin letters

D_c - external diameter of the concrete element
E_1 – elastic stiffness
E_2 – cracked stiffness
E_s - elastic steel modulus
E_{sh} - plastic steel modulus
F - load
F_{cr} - cracking load
F_y - yield load
F_u - ultimate load/peak load
K_c - shape of the deviatoric plane
L_b – effective rebar length ($=L_c+4d_b$)
L_c – coupler length
Ø - diameter

Figures

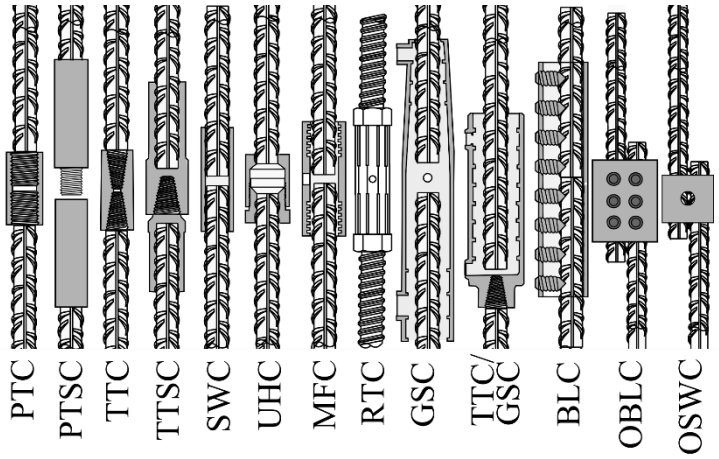


Figure 1 *a) Coupler systems: (Threaded: PTC Parallel threaded, TTC Taper threaded, PTSC Cold forged sleeve with parallel threads, TTSC Cold forged sleeve with taper threads, TTWC Taper threads from welded heads), (Swaged: SWC Swaged, OSWC Offset wedge swaged, BLC Bolt lock, OBLC Offset bolt lock), (Grouted: GSC Grouted sleeve, TTC/GSC Taper threaded-Grouted sleeve), (Other systems: UHC Upset headed, MFC Metal filled, RTC Rib thread);*

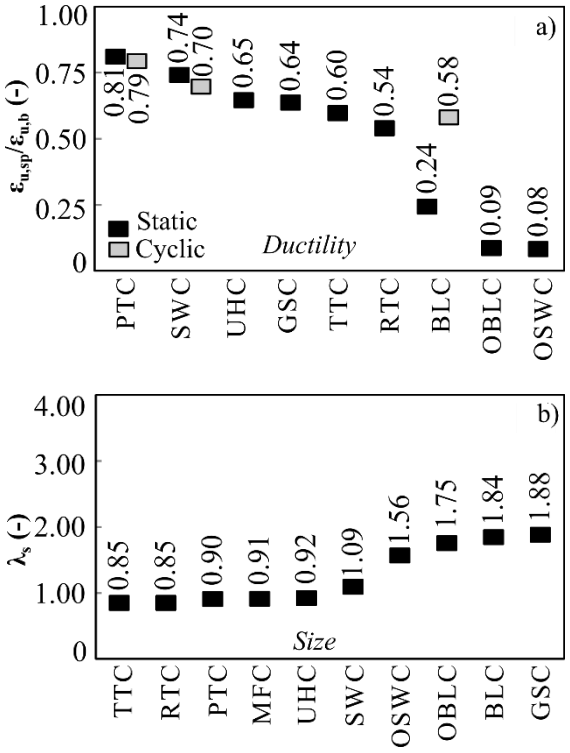


Figure 2 *a) ductility criteria; b) average size factor* λ_s

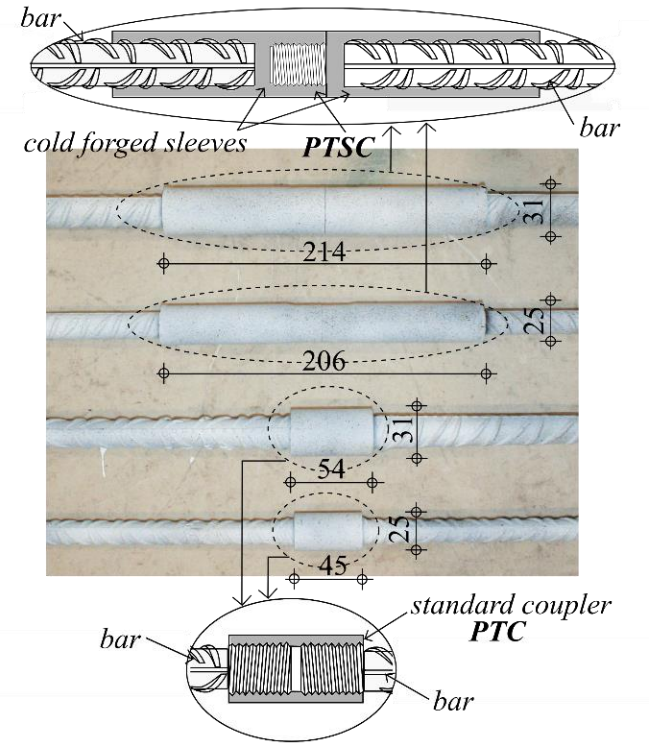


Figure 3 *Uniaxial in-air sample configurations for PTC and PTSC couplers with 16mm and 20mm rebars*

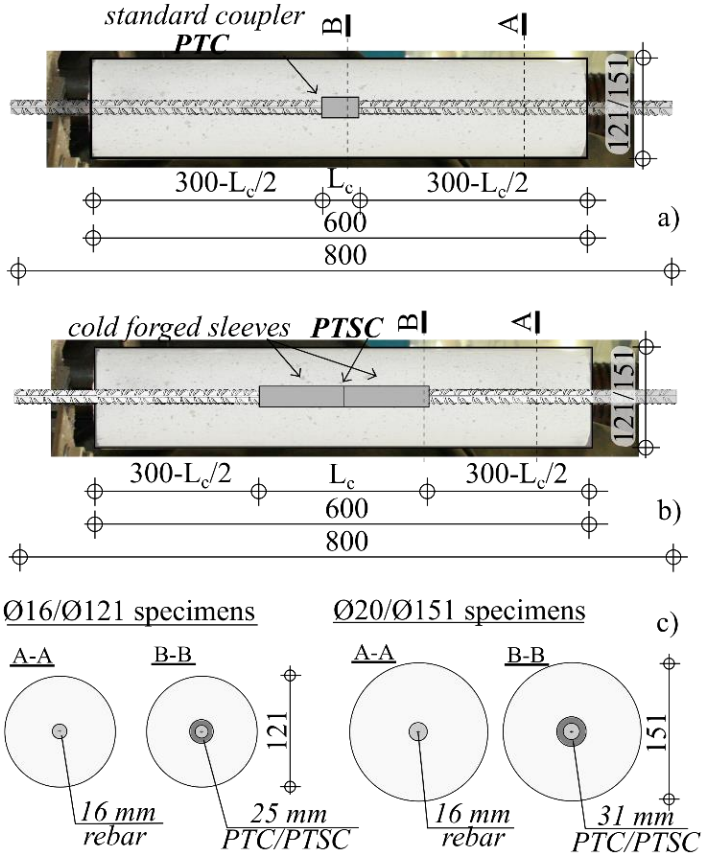


Figure 4 *In-concrete specimens: a) with PTC, b) with PTSC, c) cross-sections through members*



Figure 5 *Reinforcement bar details*

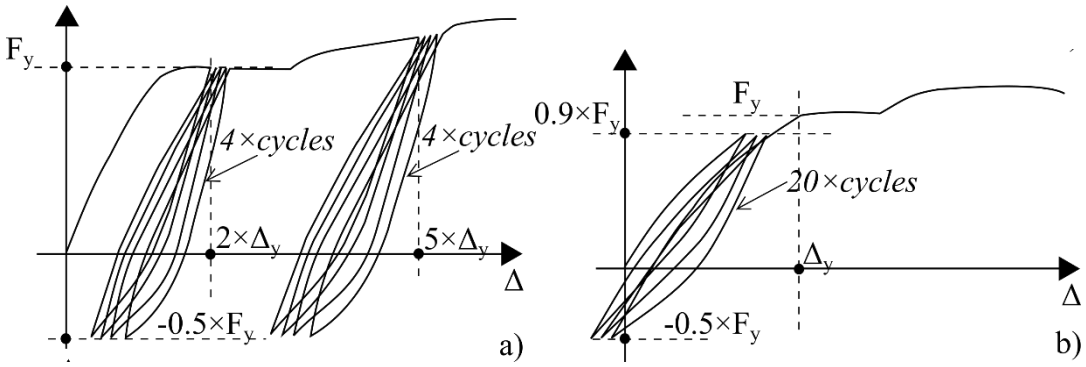


Figure 6 *Schematic representation of the loading procedures ISO 15835-2:2009 [9]: a) S2 inelastic cyclic, b) S1 elastic cyclic*

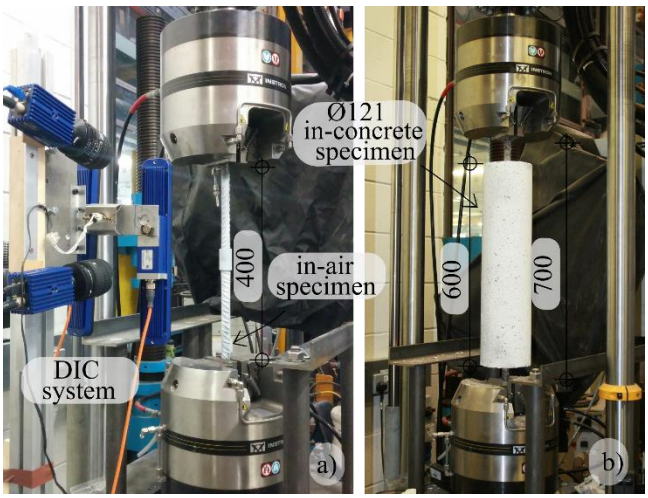


Figure 7 *Testing machine with: a) in-air sample, b) in-concrete specimen*

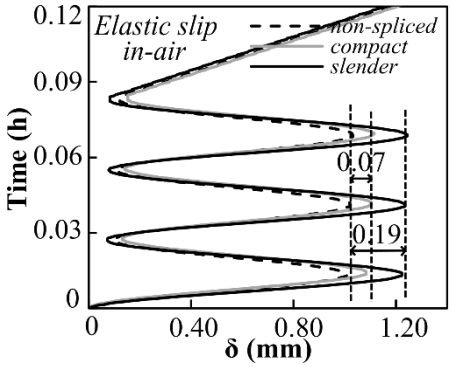


Figure 8 *Elastic slip results*

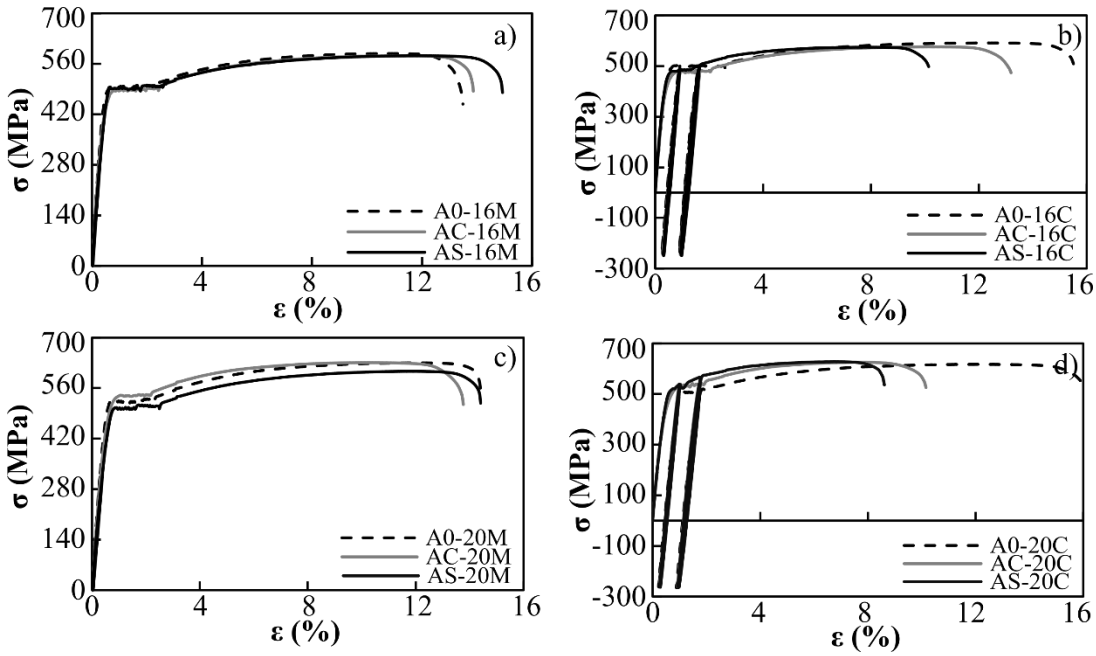


Figure 9 *σ-ε relationships for in-air tests: a) 16 mm monotonic, b) 16 mm cyclic, c) 20 mm monotonic, d) 20 mm cyclic*

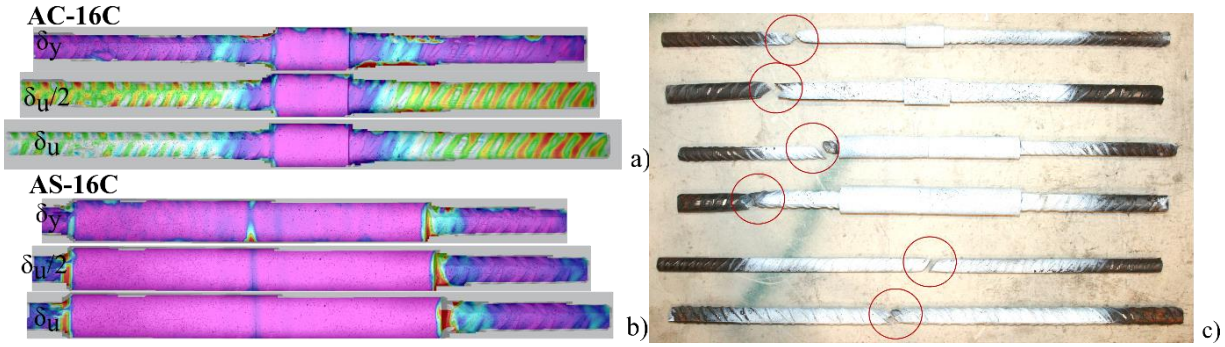


Figure 10 *Longitudinal strains at yield, half ultimate and ultimate applied deformation for a) AC-16C, b) AS-16C; c) failure location of investigated cyclic specimens*

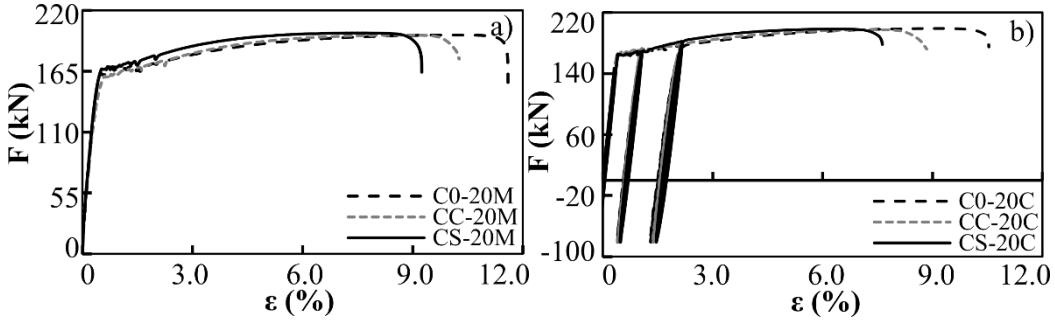


Figure 11 *F - ε response for in-concrete members provided with 20 mm bars a) monotonic tests, b) cyclic tests.*

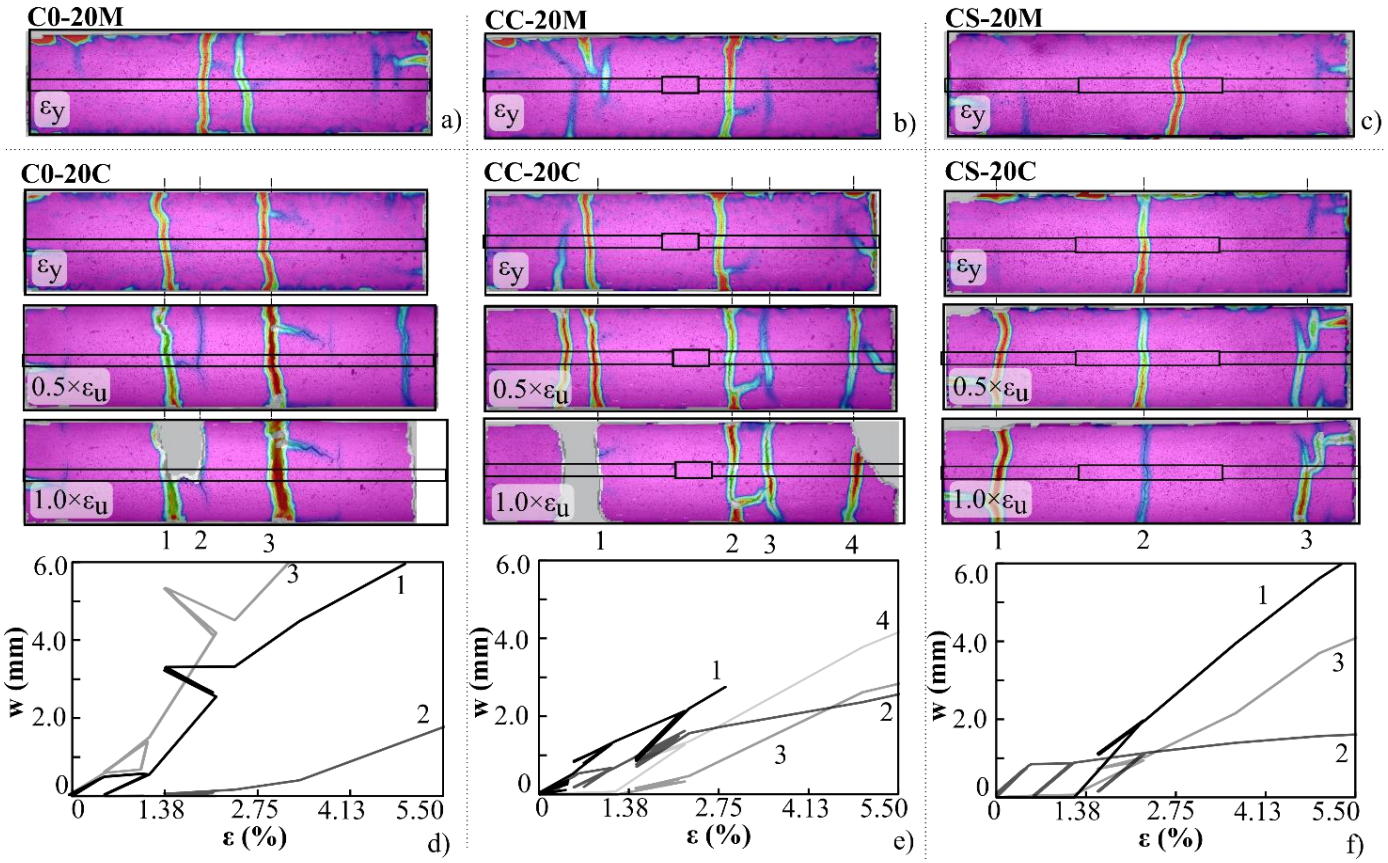


Figure 12 *Crack pattern and crack widths for in-concrete members provided with 20 mm bars: monotonic tests a) C0-20M, b) CC-20M, c) CS-20M; cyclic tests d) C0-20C, e) CC-20C, f) CS-20C*

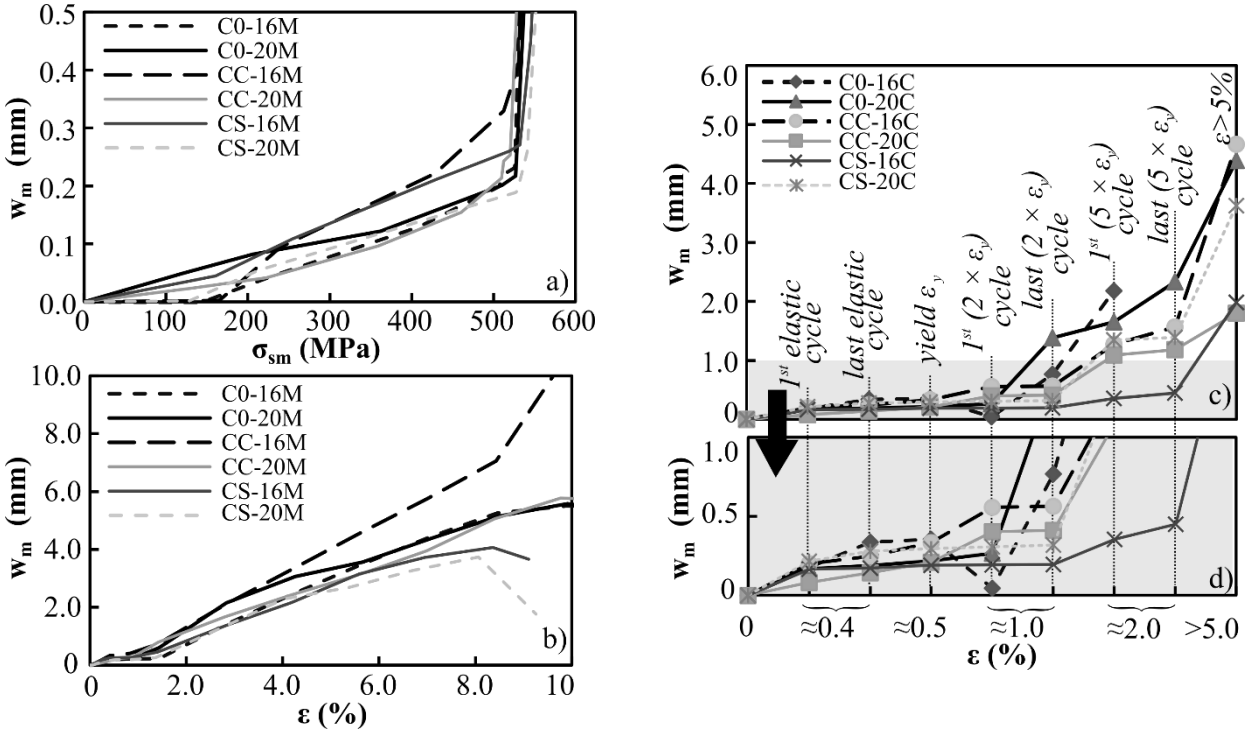


Figure 13 *a) Average crack width w_m vs reinforcement stress σ_{sm}, b) average crack width w_m vs member mean strain ε for in-concrete monotonic tests; c,d) average crack width w_m vs member mean strain ε for in-concrete cyclic tests*

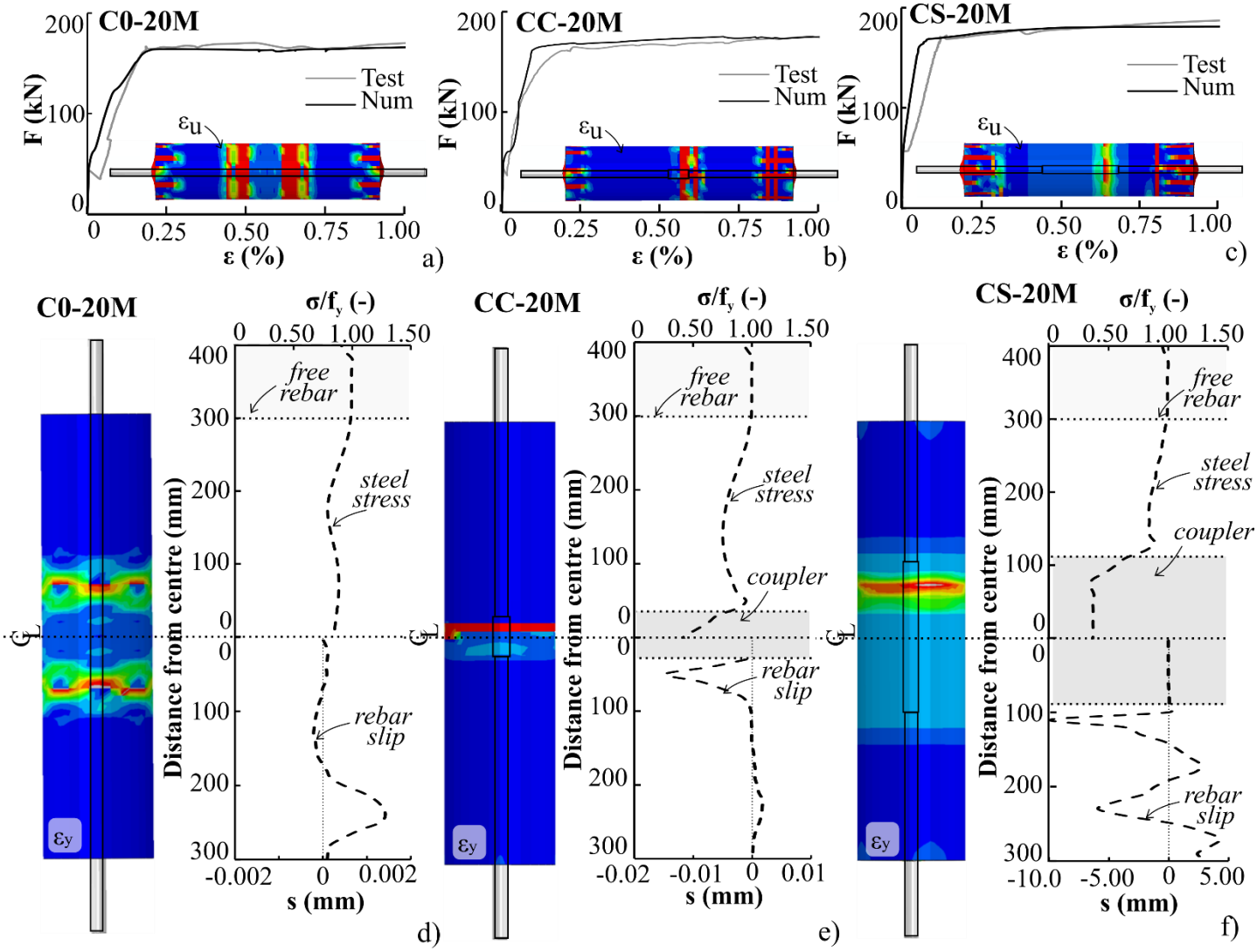


Figure 14 *Numerical validation of F-ε responses for: a) C0-20M, b) CC-20M, c) CS-20M; Steel stress σ_{sm} and slip s distributions for in-concrete models at yield for: d) non-spliced model C0-20M, e) CC-20M with compact coupler, f) CS-20M with slender coupler*

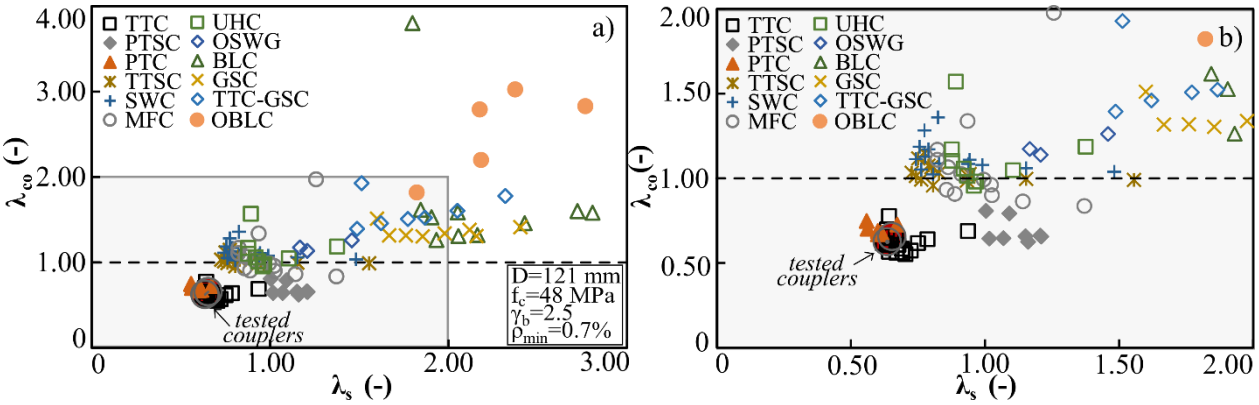


Figure 15 *Relationship between slenderness ratio λ_s and crack spacing ratio λ_{co}*

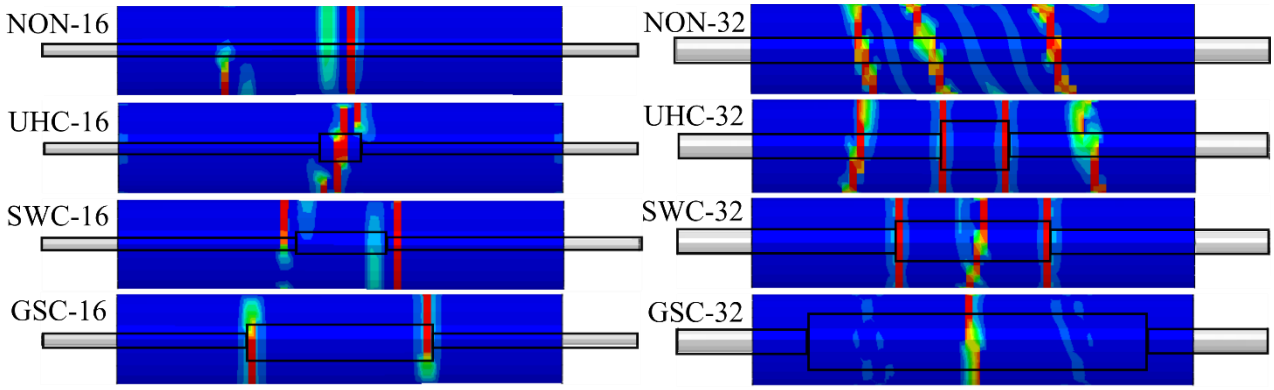


Figure 16 *Crack patterns for 16 mm and 32 mm non-spliced models and models incorporating splices with UHC, SWC, GSC*

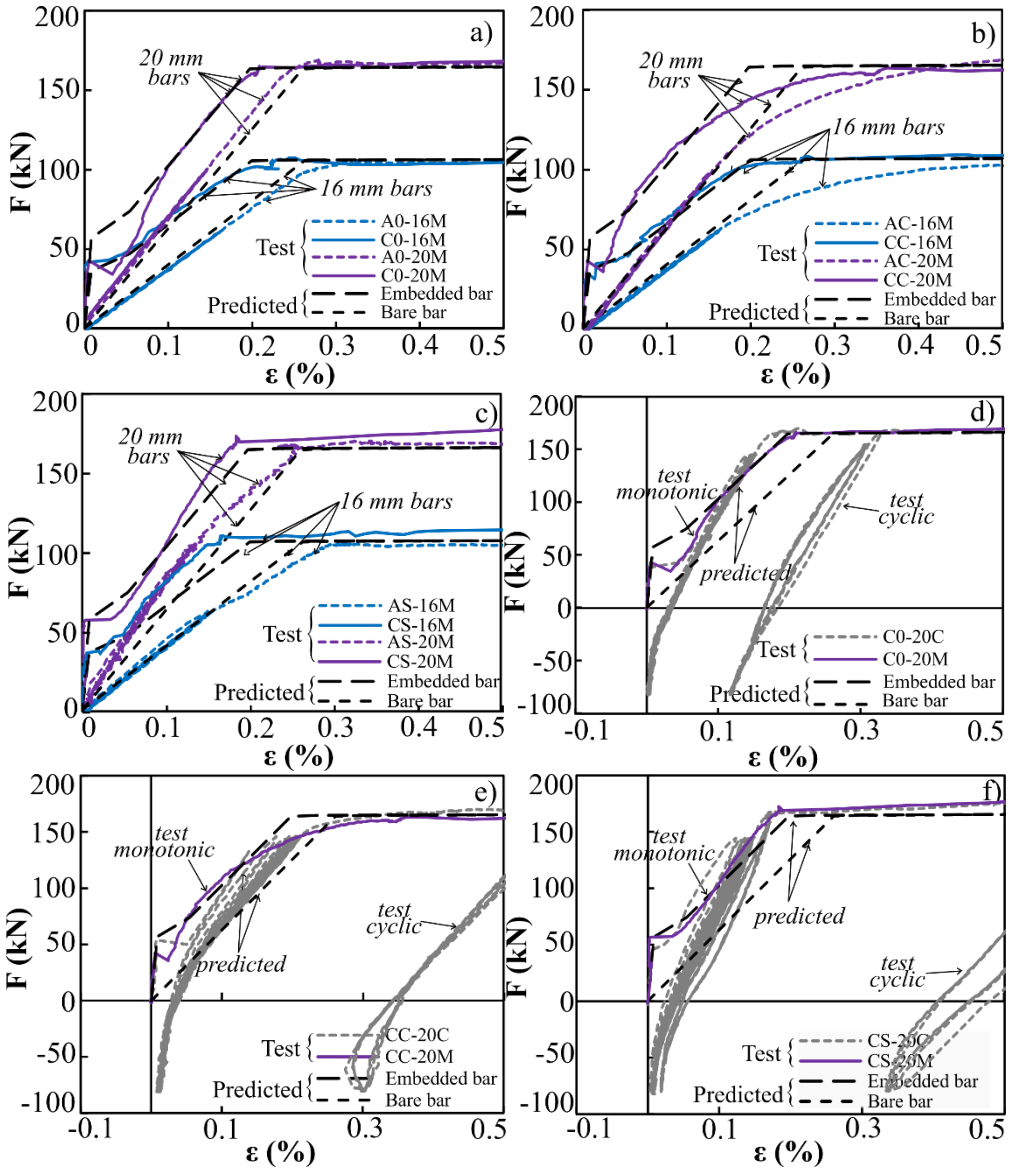


Figure 17 *Test and predicted F-ε responses for monotonic in-air and in-concrete members incorporating 16 mm and 20 mm rebars: a) non-spliced specimens, b) with compact couplers, c) with slender couplers; cyclic in-concrete members incorporating 20 mm rebars for member: d) without couplers, d) with compact couplers, e) with slender couplers*

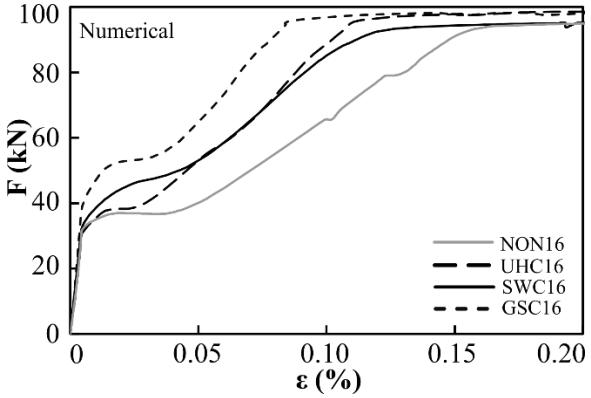


Figure 18 *F-ε for 16 mm non-spliced models and models with UHC, SWC and GSC*

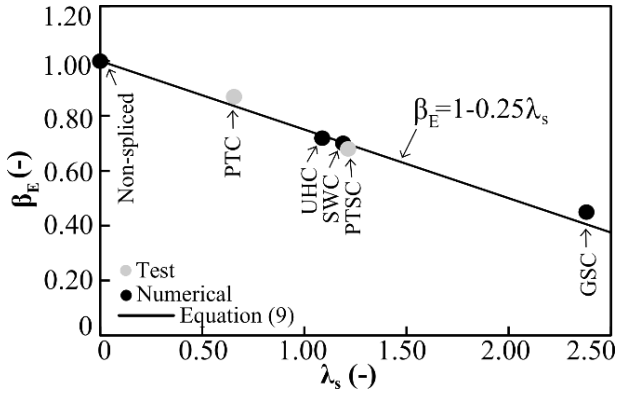


Figure 19 *Relationship between stiffness reduction factor β_E and size factor λ_s*

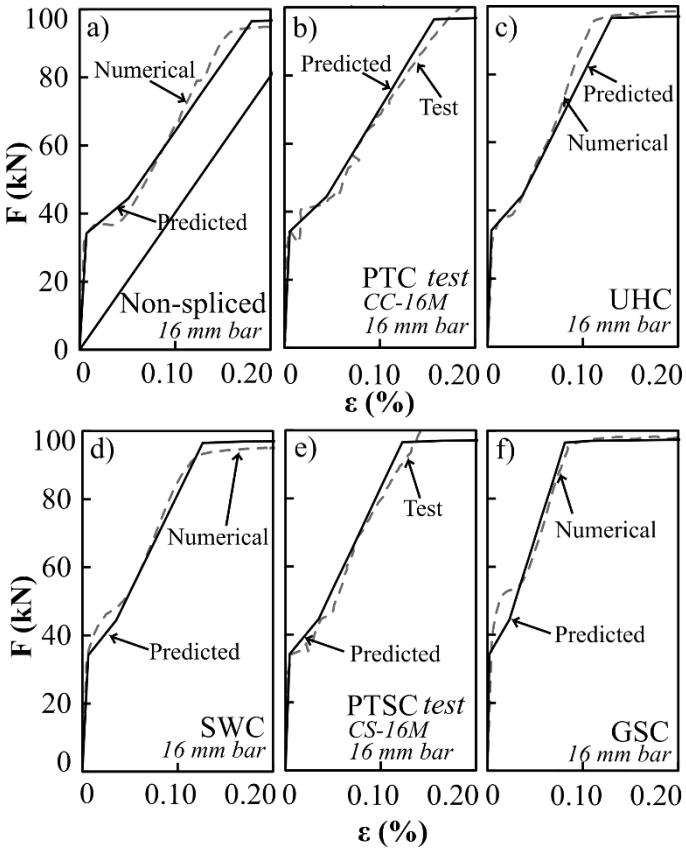


Figure 20 *Predictions of F-ε response by considering cracked stiffness reduction factor β_E*

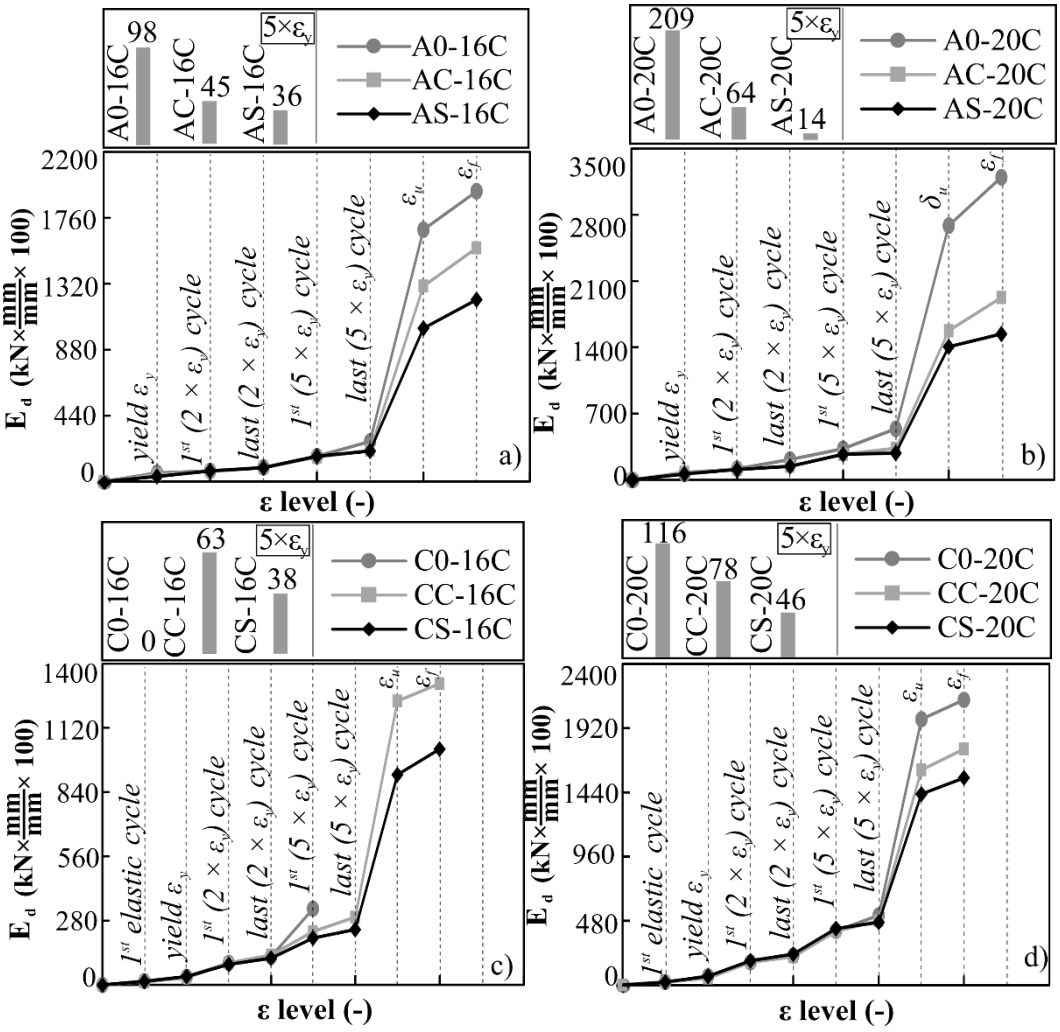


Figure 21 *Energy dissipation for in-air specimens a) 16 mm, b) 20 mm; in-concrete specimens c) 16 mm, d) 20 mm*

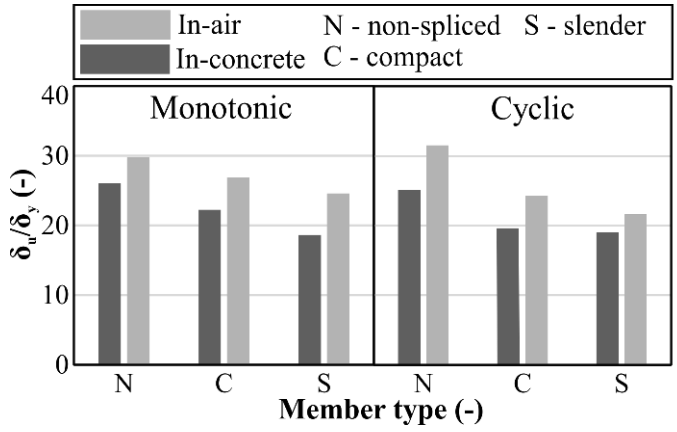


Figure 22 *Ductility comparisons for: a) monotonic tests, b) cyclic tests*

Tables

Table 1 Details of test specimens

	In-air tests			In-concrete tests			
Type	d_b	Specimen	TP	d_b	D_c	Specimen	TP
non-spliced	16	A0-16M	M	16	121	C0-16M	M
	16	A0-16C	S2	16	121	C0-16C	S1+S2
	20	A0-20M	M	20	151	C0-20M	M
	20	A0-20C	S2	20	151	C0-20M	S1+S2
compact	16	AC-16M	M	16	121	CC-16M	M
	16	AC-16C	S2	16	121	CC-16C	S1+S2
	20	AC-20M	M	20	151	CC-20M	M
	20	AC-20C	S2	20	151	CC-20C	S1+S2
slender	16	AS-16M	M	16	121	CS-16M	M
	16	AS-16C	S2	16	121	CS-16C	S1+S2
	20	AS-20M	M	20	151	CS-20M	M
	20	AS-20C	S2	20	151	CS-20C	S1+S2

TP – test protocol (M - monotonic, S2 – inelastic cyclic, S1 + S2 – elastic and inelastic cyclic)

Table 2 Test results of uniaxial in-air rebar tests

Name	F_y (kN)	F_u (kN)	f_y (MPa)	f_u (MPa)	ε_y (%)	ε_u (%)	ε_f (%)	μ_ε (-)
A0-16M	105	125	524	620	0.39	11.7	13.5	30
A0-16C	106	126	529	624	0.40	13.4	15.5	34
A0-20M	160	194	509	617	0.42	12.7	14.4	30
A0-20C	160	194	508	617	0.45	13.3	16.0	30
AC-16M	104	124	515	614	0.40	12.2	13.9	31
AC-16C	102	122	506	608	0.37	11.0	13.2	30
AC-20M	173	202	549	643	0.49	11.4	13.8	23
AC-20C	168	197	536	625	0.45	8.3	10.3	18
AS-16M	104	123	518	613	0.47	13.0	14.9	28
AS-16C	102	122	509	606	0.34	8.5	10.2	25
AS-20M	163	194	518	617	0.57	12.3	14.4	22
AS-20C	161	197	513	627	0.39	7.2	8.6	18

Table 3 Test results of concrete members

Name	F_{cr} (kN)	F_y (kN)	F_u (kN)	ε_y (%)	ε_u (%)	ε_f (%)	E_1 (kNmm/mm)	E_2 (kNmm/mm)	μ_ε
C0-16M	31	105	125	0.40	11.3	12.3	42855	26225	28
C0-16C	48	117	123	0.42	2.7	2.7	54858	28056	B
C0-20M	44	161	197	0.47	11.2	11.6	79974	33934	24
C0-20C	-	165	199	0.39	9.80	10.5	45587	41753	25
CC-16M	28	103	125	0.40	11.1	11.8	65089	26057	28
CC-16C	-	105	125	0.50	9.7	10.3	33632	10910	19
CC-20M	43	160	198	0.55	9.2	10.3	77518	28959	17
CC-20C	-	168	197	0.40	8.0	8.8	46617	41712	20
CS-16M	30	105	126	0.38	8.0	9.1	62689	27684	21
CS-16C	-	105	126	0.33	7.1	8.0	35004	31704	21
CS-20M	35	166	200	0.49	7.9	9.3	62832	34170	16
CS-20C	-	164	198	0.42	7.0	7.7	47320	39552	17

Table 4 Crack spacing

Specimen	at rebar yield ε_y						at ultimate ε_u					
	n_{cr}	s_{rmin}	s_{rm}	s_{rmax}	s_{rmin}/s_{rm}	s_{rmax}/s_{rm}	n_{cr}	s_{rmin}	s_{rm}	s_{rmax}	s_{rmin}/s_{rm}	s_{rmax}/s_{rm}
C0-16M	2	97	199	253	0.49	1.27	5	64	100	189	0.64	1.89
C0-20M	2	65	198	274	0.33	1.38	5	56	100	176	0.56	1.76
C0-16C	2	157	197	261	0.80	1.33	3	73	150	190	0.49	1.27
C0-20C	2	142	198	244	0.72	1.23	3	50	150	210	0.33	1.40
	Average C0				0.58	1.30	Average C0				0.50	1.58
CC-16M	2	151	200	268	0.75	1.34	4	45	120	194	0.38	1.61
CC-20M	2	137	199	233	0.69	1.17	5	55	100	230	0.55	2.30
CC-16C	3	63	149	212	0.43	1.42	5	51	100	152	0.51	1.52
CC-20C	2	156	198	241	0.79	1.22	5	45	100	200	0.45	2.00
	Average CC				0.66	1.29	Average CC				0.47	1.86
CS-16M	2	192	200	212	0.96	1.06	5	56	100	208	0.56	2.08
CS-20M	2	110	197	254	0.56	1.29	3	67	150	220	0.45	1.47
CS-16C	2	134	200	248	0.67	1.24	4	58	120	172	0.48	1.44
CS-20C	2	54	197	294	0.28	1.49	3	71	150	230	0.47	1.53
	Average CS				0.62	1.27	Average CS				0.49	1.63
	Average all				0.62	1.29	Average all				0.49	1.69